Human Molecular Genetics, 2013, Vol. 22, No. 17 ***3397–3414***
doi:10.1093/hmg/ddt190
Advance Access published on April 24, 2013

Missense mutation in mouse GALC mimics human gene defect and offers new insights into Krabbe disease

Gregory B. Potter[1,2,5,*], Marta Santos[3], Muriel T. Davisson[4], David H. Rowitch[5], Dan L. Marks[1,2], Ernesto R. Bongarzone[3] and Magdalena A. Petryniak[1,2,5,*]

[1]Department of Pediatrics, Oregon Health & Science University, Portland, OR 97239, USA, [2]Papé Family Pediatric Research Institute, [3]The Myelin Regeneration Group at the Department Anatomy & Cell Biology, University of Illinois, Chicago, The Myelin Regeneration Group at the Dept. Anatomy & Cell Biology, Chicago, IL, [4]The Jackson Laboratory, Genetic Resource Science, 600 Main St., Bar Harbor, ME 04609 and [5]Department of Pediatrics and Howard Hughes Medical Institute, University of California, San Francisco, CA, USA

Received March 15, 2013; Revised April 9, 2013; Accepted April 22, 2013

Krabbe disease is a devastating pediatric leukodystrophy caused by mutations in the galactocerebrosidase (*GALC*) gene. A significant subset of the infantile form of the disease is due to missense mutations that result in aberrant protein production. The currently used mouse model, twitcher, has a nonsense mutation not found in Krabbe patients, although it is similar to the human 30 kb deletion in abrogating GALC expression. Here, we identify a spontaneous mutation in GALC, *GALC*$^{twi-5J}$, that precisely matches the E130K missense mutation in patients with infantile Krabbe disease. *GALC*$^{twi-5J}$ homozygotes show loss of enzymatic activity despite normal levels of precursor protein, and manifest a more severe phenotype than twitcher, with half the life span. Although neuropathological hallmarks such as gliosis, globoid cells and psychosine accumulation are present throughout the nervous system, the CNS does not manifest significant demyelination. In contrast, the PNS is severely hypomyelinated and lacks large diameter axons, suggesting primary dysmyelination, rather than a demyelinating process. Our data indicate that early demise is due to mechanisms other than myelin loss and support an important role for neuroinflammation in Krabbe disease progression. Furthermore, our results argue against a causative relationship between psychosine accumulation, white matter loss and gliosis.

INTRODUCTION

Krabbe disease, also known as globoid cell leukodystrophy (GLD), is a rare, autosomal recessive disorder caused by mutations in the gene coding for the lysosomal enzyme galactocerebrosidase (GALC). GALC is responsible for catabolism of galactocerebroside; enzymatic deficiency results in accumulation of the metabolite psychosine, which is proposed to be cytotoxic to oligodendrocytes, the myelin-producing cells of the central nervous system (CNS) (1,2). Schwann cells, the myelin-forming cells of the peripheral nervous system (PNS), may degenerate in the presence of psychosine *in vivo* and their ability to form or turn over myelin is hindered by GALC enzymatic deficiency (3,4). A common mutant allele, found in 35–50% of Krabbe patients of European ancestry, is a 30 kb deletion (502T/del) of *GALC* (5,6); the majority of other *GALC* alleles associated with Krabbe disease are missense mutations that occur outside of the enzymatic domain (7–9) and cause loss of enzymatic activity that may be attributable to abnormal protein processing, localization or degradation (10). Classical pathological features of the infantile form of the disease include variable loss of peripheral or central myelin, axonal degeneration, presence of globoid cells and gliosis of the cerebrum and white matter (11). Approximately 90% of patients present with the infantile form of the disease and generally die by 2 years of age (11). Treatment for Krabbe disease is symptomatic and supportive. There is presently no cure and hematopoietic stem-cell transplantation therapy is of limited benefit (12). The

*To whom correspondence should be addressed at: Department of Pediatrics, Oregon Health and Science University, 3181 SW Sam Jackson Park Rd, L321, Portland, OR 97329, USA. Tel: +1 5034945745; Fax: +1 5034185044; Email: pottergr@ohsu.edu (G.B.P.); petrynia@ohsu.edu (M.A.P.)

use of animal models is therefore crucial for enhanced understanding of disease mechanisms as well as developing new therapeutic approaches for Krabbe disease.

Currently, the most widely used mouse model of Krabbe disease is the twitcher strain. The twitcher ($Galc^{twi}$) mutation arose spontaneously at The Jackson Laboratory (JAX) in 1976, and results in nonsense-mediated mRNA decay of the truncated *Galc* transcript and elimination of GALC protein expression (13,14). Twitcher mice have phenotypic features such as hindlimb weakness and weight loss, and histopathological signs, including nervous system gliosis, myelin loss and macrophage accumulation, akin to human Krabbe disease (15,16). However, disease progression in twitcher is relatively slow with death after 6 weeks. Furthermore, while a subset of infantile Krabbe patients have nonsense mutations in *GALC*, the twitcher mutation is not present in human patients (5). Nevertheless, twitcher is used as a surrogate model of the common 502T/del mutant allele, as both alleles exhibit loss of GALC protein expression. An engineered transgenic mouse strain, $GALC^{trs}$, contains a targeted mutation in GALC and presents with a milder phenotype due to aberrant splicing, thus inadequately modeling early-onset Krabbe disease (17).

In this report, we identify and describe a spontaneous missense mutation in mouse *Galc* ($Galc^{twi\text{-}5J}$) that is identical to a mutation present in a subset of patients with infantile Krabbe disease. We characterize the expression of mutant GALC in the mouse nervous system and show that the missense mutation abolishes enzymatic activity without loss of GALC precursor protein expression. Mice homozygous for $Galc^{twi\text{-}5J}$ (hereafter referred to as twi-5J) exhibit neuropathological hallmarks representative of infantile Krabbe disease including globoid cell and psychosine accumulation, and manifest a more severe phenotype than twitcher with death during the fourth post-natal week. Surprisingly, we find that CNS regions with the highest psychosine levels show no detectable evidence of dysmyelination or axonal loss, suggesting that psychosine accumulation does not necessarily or directly lead to myelin loss. Furthermore, twi-5J exhibit profound PNS hypomyelination in association with marked loss of large caliber axons, indicating a primary axonopathy rather than demyelinating process.

Our data demonstrate that twi-5J represent a class of Krabbe patients with missense alleles and indicate twi-5J are an important addition to the twitcher mouse model in understanding the pathogenesis of Krabbe disease.

RESULTS

Identification of a new mutation in *Galc* resulting in severe early-onset phenotype

Twitcher do not show any obvious clinical manifestations during the first 3 weeks after birth, but subsequently exhibit neurological symptoms, including ataxia, tremulousness and hindlimb paralysis. We identified a new mutant with a phenotype similar to twitcher that arose spontaneously in The Jackson Laboratory Production colony of strain BXD32/TyJ. Mice homozygous for the new mutation manifest generalized tremors and a smaller body size after 2 weeks of age. They exhibit weakness, stunted weight gain and die sooner than twitcher with a median survival of 23.5 days ($n = 22$ twi-5J, Fig. 1A and B) compared with ~43 days for twitcher (4,15).

Identification of missense mutation in *Galc* for twi-5J

To investigate the mechanism by which GALC is disrupted, we sought to identify the genetic mutation in the *Galc* gene. We sequenced all exons of *Galc* from two mutant and three unaffected littermates, and identified one non-synonymous change in exon 4, a guanine-to-adenine substitution at position 388 (G388A) (Supplementary Material, Fig. S1). This mutation is the fifth to occur at JAX in *Galc* and the allele was named *twi-5J*.

We developed a single nucleotide specific PCR assay to identify the allele before the onset of symptoms. Of 22 mutants identified based on phenotypic symptoms, all were homozygous for the 388A substitution, while animals without this phenotype were always wild-type or heterozygotes (Fig. 1C). To test whether this substitution could be a strain-specific single-nucleotide polymorphism, we performed PCR genotyping on additional strains of mice, including CD-1, C57BL/6J and 129X1/SvJ. All strains of mice have the G allele, strongly

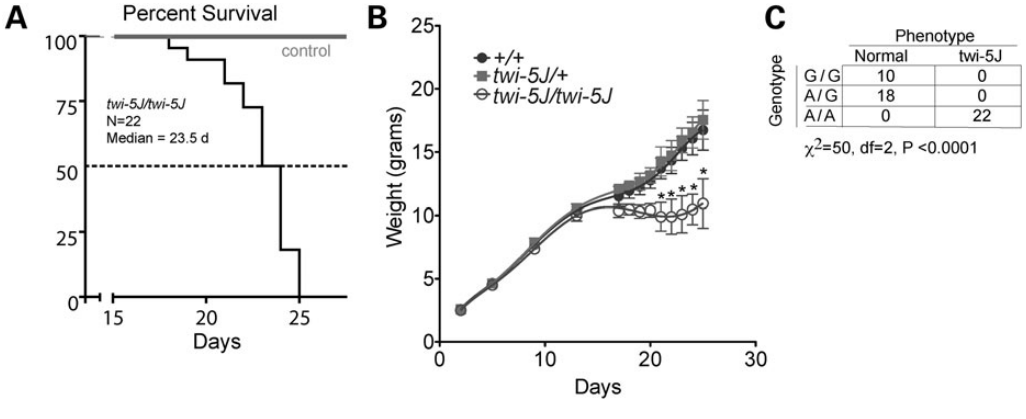

Figure 1. A missense mutation in *Galc* associates with the twi-5J phenotype. (**A**) Kaplan–Meier survival analysis of twi-5J. The median survival was 23.5 days ($n = 22$). (**B**) Weight curve of twi-5J. Homozygous $GALC^{twi\text{-}5J}$ mice weighed significantly less than heterozygotes for $GALC^{twi\text{-}5J}$ and wild-type mice after P20. $^{*}P < 0.01$. (**C**) Mice homozygous for 388A are twi-5J. Genotype analysis using allele-specific PCR to *GALC* nucleotide 388 compared with phenotype. Wild-type (G/G) and heterozygous (G/A) mice are unaffected, while all homozygous (A/A) mice show neurological symptoms and are phenotypic twi-5J.

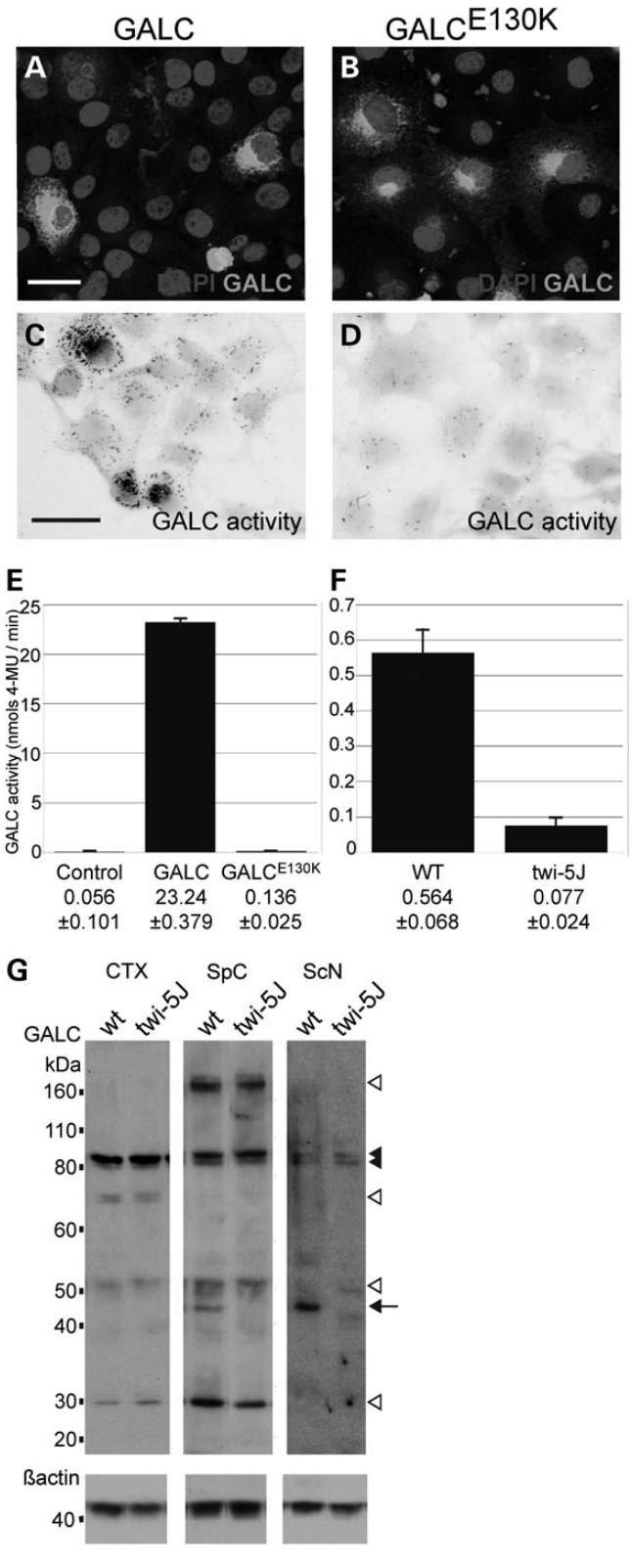

Figure 2. The E130K substitution in GALC abolishes GALC enzymatic activity without affecting precursor protein levels *in vivo*. (**A**–**D**) COS-7 cells were transfected with an expression construct for GALC (A and C) or GALC^{E130K} (B and D). (A and B) GALC (white) was detected by immunofluorescence using a GALC-specific antibody. (C and D) GALC activity (black) was visualized using a GALC histochemical assay. Cell bodies are false-colored grey. Scale bar in A, $C = 50$ μm. (**E**) GALC activity (nmols/min) was measured from 15 μg of COS-7 cells extracts transfected with expression constructs for wild-type GALC or GALC^{E130K}. Controls are mock-transfected cells. (E) GALC activity (nmols/min) measured from 15 μg of whole brain extracts from WT and twi-5J. Activity is presented as mean ± SD. (**G**) Western blot analysis using an affinity purified GALC antibody on extracts from wild-type (wt) and twi-5J collected from cortex (CTX), spinal cord (SpC) and sciatic nerve (ScN). Expression of ∼80, ∼50 and ∼30 kDa GALC bands are equivalent in cortical extracts between wild-type and twi-5J ($P > 0.05$). In contrast, a ∼45 kDa band is absent in extracts collected from mutant spinal cord and sciatic nerve compared with wild-type controls ($P < 0.001$) (arrow). The ∼80 kDa GALC precursor (black arrowheads) is present in all tissues. White arrowheads point to GALC species differentially regulated between tissues. Blots were re-probed using a beta-actin antibody to control for protein loading. Apparent molecular mass is indicated on the left. Extracts from three independent wild-type and twi-5J animals were analyzed with equivalent results; a representative immunoblot is shown.

indicating that the 388A nucleotide substitution is specific for the twi-5J mutant (data not shown).

Galc has two potential start ATG codons; we use current mutation nomenclature guidelines (http://www.hgvs.org/mutnomen), assigning the A of the first ATG translational initiation codon as nucleotide +1 when describing this mutation. The nucleotide change causes a missense mutation in which glutamic acid at amino acid position 130 is converted to a lysine (E130K) outside the catalytic domain of GALC. Notably, the E130K missense mutation has been identified in patients with the infantile form of Krabbe disease (8). A comparison of the GALC amino acid sequence across vertebrate species at position 130 indicates that the glutamic acid is 100% conserved. Indeed, amino acids 122–142 are identical across all vertebrate species examined, indicating strict evolutionary conservation of this motif and suggesting an important role in protein function.

The E130K mutation causes loss of GALC enzymatic activity

To test if the E130K substitution affects the enzymatic activity of GALC, we generated expression constructs for wild-type GALC and GALC^{E130K}. The expression constructs were transfected into COS-7 cells and GALC activity was detected using a GALC histochemical assay (18). Wild-type GALC and GALC^{E130K} showed similar distribution within transfected COS-7 cells but only GALC exhibited strong enzymatic activity (Fig. 2A–D). To quantify changes in enzymatic activity, we measured GALC enzymatic activity from whole cell extracts using a modified X-gal assay as previously described (Fig. 2E) (19). Non-transfected cells exhibited very low levels of enzymatic activity. Extracts from GALC-transfected cells exhibited a substantial level of enzymatic activity, roughly 415 times greater than mock-transfected cells ($P < 0.001, n = 3$) while enzymatic activity measured from GALC^{E130K} expressing cells was <1% of wild-type GALC (∼0.58% of wild-type activity, $P < 0.001$, $n = 3$). Activity levels between GALC^{E130K}-transfected cells and mock-transfected cells were not significantly different ($P > 0.05$). Furthermore, whole brain extracts from twi-5J exhibited significantly lower GALC enzymatic activity than wild-type mice, with a >7-fold decrease down to the detection sensitivity of assay ($P < 0.001, n = 3$) (Fig. 2F). Taken together, these data indicate that the E130K substitution in GALC abolishes its enzymatic activity *in vivo*.

GALC expression differs between regions of the mouse nervous system and is distinctly affected in twi-5J

To examine the effect of the E130K mutation on GALC protein expression, we performed immunoblots on extracts collected from cortex, spinal cord and sciatic nerve of wild-type and twi-5J using an affinity purified GALC antibody (Fig. 2G) (10). GALC is expressed as a ~80 kDa precursor that is processed in lysosomes into two fragments, ~50 kDa N-terminal and ~30 kDa C-terminal fragments. GALC enzymatic activity *in vitro* has been correlated with the expression of the 80 kDa precursor, and the processed isoforms are predicted to stabilize the 80 kDa protein (20,21). Western blot analysis revealed that various species of GALC are differentially detectable throughout the nervous system, suggesting region-specific post-translational modifications, such as glycosylation or phosphorylation, could further vary the apparent molecular mass of the GALC isoforms. A doublet band around 80 kDa was detected in both the CNS and PNS, while 50 and 30 kDa bands were detected in cortex and spinal cord, but not sciatic nerve. A band ~170 kDa was detected in spinal cord, but not cortex or sciatic nerve; this larger band may be a dimer or larger aggregate of the GALC precursor (10). In general, GALC was expressed at lower levels in the sciatic nerve compared with the cortex and spinal cord. Notably, the expression of the 80 kDa band in all tissues and the 50 and 30 kDa bands in the cortex and spinal cord were equivalent between wild-type and twi-5J extracts ($n = 3$ pairs; $P > 0.05$). Interestingly, we observed a ~45 kDa band in wild-type spinal cord, brainstem and sciatic nerve extracts, which was absent from twi-5J. This isoform was not detectable in the cortex, but was present outside the nervous system in the wild-type (Supplementary Material, Fig. S2). These data indicate that GALC expression varies between nervous system regions, which previously has not been described, and the ~45 kDa species of GALC is greatly diminished in the spinal cord, sciatic nerve and brainstem of twi-5J. Since there is no significant difference in GALC expression between control and twi-5J in the cortex, the loss of enzymatic activity detected in twi-5J is likely due to a functional defect in GALC and not to low levels of the protein.

Twi-5J have significant globoid cell accumulation and gliosis in the CNS, but limited myelin loss

Globoid cell accumulation and astrocytic gliosis are hallmarks of GALC deficiency and Krabbe disease (22,23). We detected early signs of reactive astrocytosis and few Iba-1-expressing macrophages in the forebrain and spinal cord in twi-5J at P15 (Supplementary Material, Fig. S3). By 3 weeks of age, there was extensive gliosis in the forebrain and brainstem, with reactive GFAP-expressing astrocytes evident in the cortex, septum and corpus callosum (Fig. 3A and B and data not shown). Reactive astrocytes were also evident within the pyramidal tracts, cuneate fasciculus and dorsal white matter of the spinal cord, and were especially prominent at the dorsal root entry and ventral root exit zones (Fig. 4B–E). The presence of reactive astrocytes in the CNS at terminal timepoints was accompanied by marked globoid cell infiltration, as revealed by Iba-1 immunohistochemistry (Figs 3C and D and 4F–I). Further examination of the inflammatory response in the CNS at both early and terminal stages of the disease revealed significant up-regulation of LIF and IL-1β gene expression throughout the CNS at P25, but not at P15, in the cortex, brainstem and spinal cord of twi-5J compared with wild-type (Fig. 5A). Interestingly, changes in LIF levels exceeded IL-1β in the CNS, and this cytokine was dramatically up-regulated, ~100 fold, in the cortex of twi-5J.

It has been postulated that globoid cell accumulation is coincident with demyelination as macrophages remove myelin debris, although the mechanism of macrophage recruitment is still unresolved (23,24). We sought to determine if CNS myelin loss accompanies the robust inflammatory response we observed in twi-5J animals by examining the immunohistochemical pattern of myelin basic protein (MBP) expression as well as levels of MBP isoforms in the forebrain, brainstem, cerebellum and spinal cord at P15 and P25 (Figs 3E–H and 4J–L and Supplementary Material, Fig. S3). Surprisingly, MBP immuno-staining appears comparable to wild-type in these structures not only at disease onset but also in terminal animals, despite neurological symptoms and impending death. However, we were able to detect significant reductions in cortical levels of all MBP isoforms by P25, whereas there was no difference in other regions of the CNS nor at earlier timepoints (Fig. 6A–C, Supplementary Material, Fig. S4). Thus, in contrast to twitcher mice that lack GALC expression, significant CNS demyelination is not evident in twi-5J despite a marked inflammatory response.

Ultrastructural analysis reveals axonal abnormalities without evidence of demyelinating process in the CNS

To examine morphology and myelination in twi-5J at the ultrastructural level, we compared the corpus callosum and spinal cord of twi-5J and wild-type by electron microscopy at P25 (Fig. 7A–F). In the corpus callosum, we analyzed the distribution of axon diameter, as well as the g-ratio (ratio of the axon diameter to myelinated axon diameter) and percentage of unmyelinated axons among medium (330–650 μm) and large (>650 nm) diameter axons. Normally, small (<330 nm) diameter axons are unmyelinated, which was the case in both wild-type and twi-5J. We observed a redistribution of axon size in the twi5-J when compared with wild-type, with a shift toward predominantly medium-sized axons and nearly a 20% reduction in the number of large diameter axons from 43.2 ± 1.4 to 36.2 ± 1.1% of the total axon population ($P < 0.05$) (Fig. 8A). Furthermore, a subgroup of medium diameter axons <400 nm have a lower g-ratio in twi-5J compared with wild-type, suggesting they are hypermyelinated ($P < 0.03$). Quantification of unmyelinated medium and large diameter axons revealed a higher, albeit still relatively small proportion of unmyelinated axons >330 nm in the twi-5J compared with the wild-type, 7.3 ± 1.7 versus 4.0 ± 1.1%, respectively ($P < 0.05$). Nevertheless, the higher proportion of unmyelinated axons in combination with the loss of large, normally heavily myelinated axons in twi-5J could account for the reduction in the MBP protein levels observed in the forebrain. In the spinal cord, the percentage of unmyelinated medium and large axons in the twi-5J was not statistically different compared with controls (5.1 ± 0.9 versus 3.4 ± 0.8%; $P = 0.07$). Likewise, there was no difference in axonal numbers or reduction in large diameter axons in the

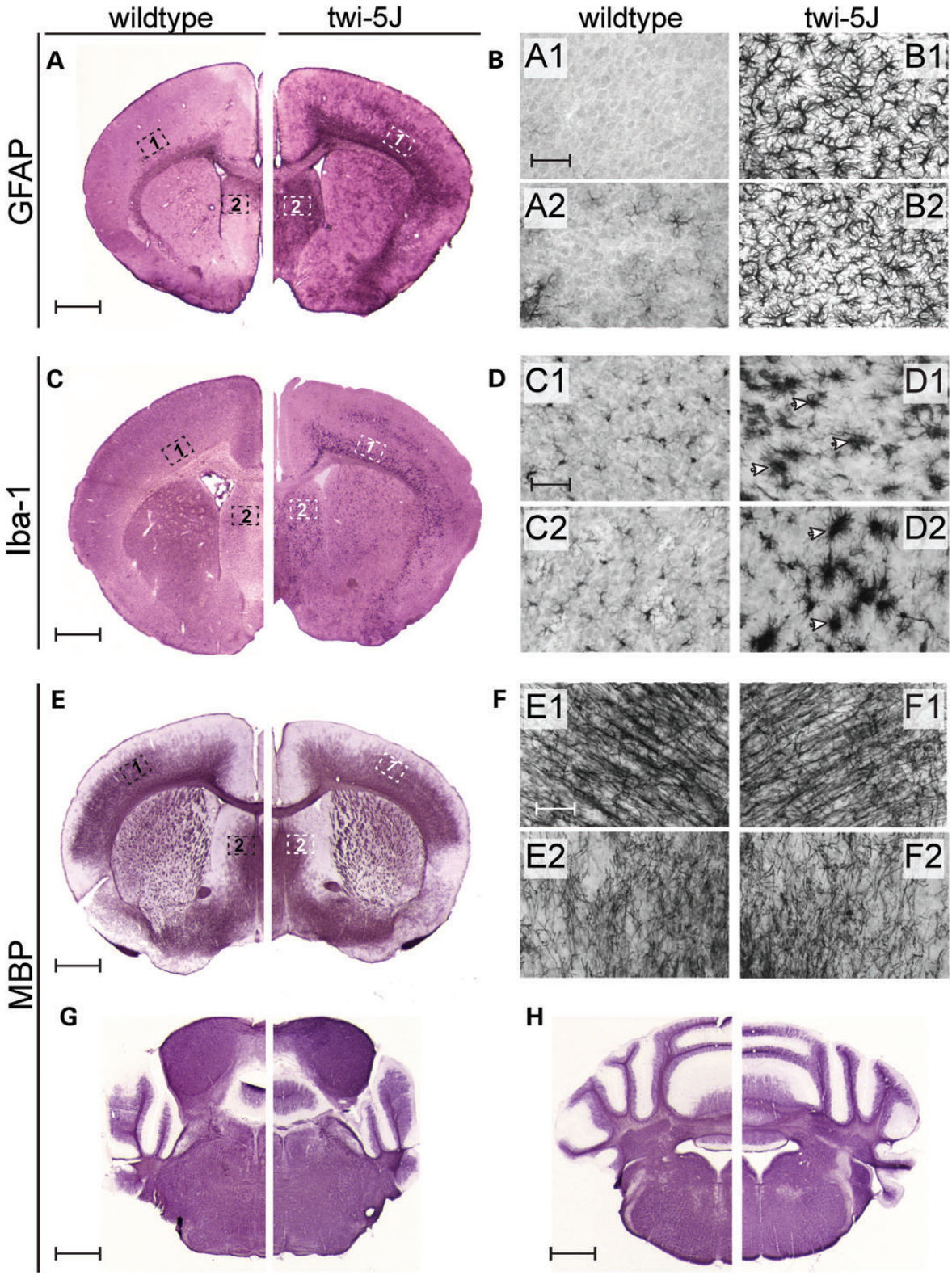

Figure 3. Twi-5J display gliosis and globoid cell accumulation in the forebrain. (**A** and **B**) GFAP immunohistochemistry on coronal sections from P25 wild-type (A) and twi-5J (B) indicate an increase in reactive astrocytes within the CNS. Higher magnification views of the cortex and septum in wild-type (A1–A2) and twi-5J (B1–B2) show the presence of large, multi-branched and densely stained cells. (**C** and **D**) Iba-1 immunohistochemistry on coronal sections from P25 wild-type (C) and twi-5J (D) reveals the presence of large macrophages (arrowheads) in the mutant cortex and striatum. (**E**–**H**) MBP immunohistochemistry on coronal sections from P25 wild-type and twi-5J reveal comparable myelination in the CNS. Higher magnification views of the cortex and striatum in wild-type (E1–E2) and twi-5J (F1–F2). Scale bars: A–H = 1 mm; A1–F1, A2–F2 = 50 μm.

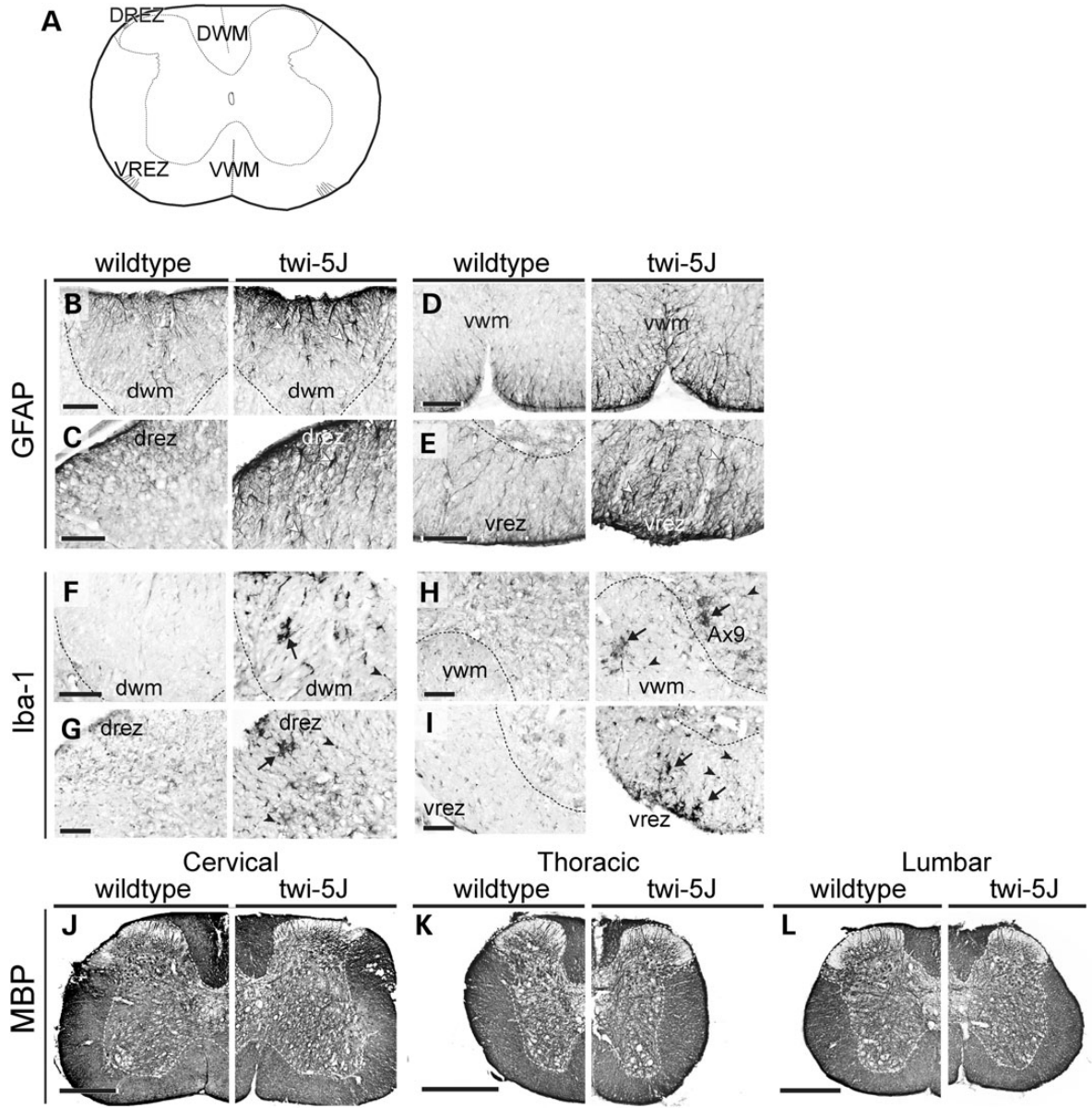

Figure 4. Spinal cords of twi-5J exhibit gliosis and macrophage accumulation. Cross-sections of spinal cords from wild-type and twi-5J were immunolabeled for GFAP (**B**–**E**), Iba-1 (**F**–**I**) and MBP (**J**–**L**). (**A**) Schematic of cross-section through spinal cord with regions of interest annotated. (B–E) Reactive astrocytes, marked by changes in astrocyte morphology and increased GFAP expression, are present in twi-5J (right panels, white arrowheads) in the dorsal (DWM) and ventral white matter (VWM) and near the dorsal root entry (drez) and ventral root exit zones (vrez). (F–I) Iba-1 immunolabeling reveals large Iba-1+ cells consistent with macrophages (arrows) and an increase in small Iba-1+ microglia (arrowhead) in ventral and dorsal white matter of twi-5J spinal cord. Ax9, lamina 9 (axial muscle innervation). (J–L) MBP expression is similar between wild-type (left) and twi-5J (right) at all levels of the spinal cord. Scale bars: B–I = 100 μm; J–L = 500 μm.

spinal cord (Fig. 8B), consistent with the normal levels of MBP expression we found in this region. However, electron-light regions were detected that could represent the earliest signs of axon loss (asterisk and white arrowhead in Fig. 7E and F, respectively.) Additionally, our EM analysis revealed lipid inclusions within axons of twi-5J in both the forebrain and spinal cord that were not observed in wild-type animals (i.e. Fig. 7C). Significantly, we did not see overt manifestations of demyelination such as shedding of myelin sheaths, or cytoplasmic changes indicative of degenerating oligodendrocytes, such as clumped nuclear chromatin, dispersed ribosomes, altered endoplasmic reticulum or increased numbers of microtubules, which are present in the twitcher spinal cord (25).

Hypomyelination and axonal loss is severe in the PNS

Peripheral neuropathy is an important feature of Krabbe disease (3,15,26). We used MBP expression, toluidine blue staining and EM to assess differences in myelination in the sciatic nerve between controls and twi-5J (Fig. 9). At P7, the size and structure of the twi-5J sciatic nerve assessed with toluidine blue staining was comparable to the wild-type. However, electron microscopy

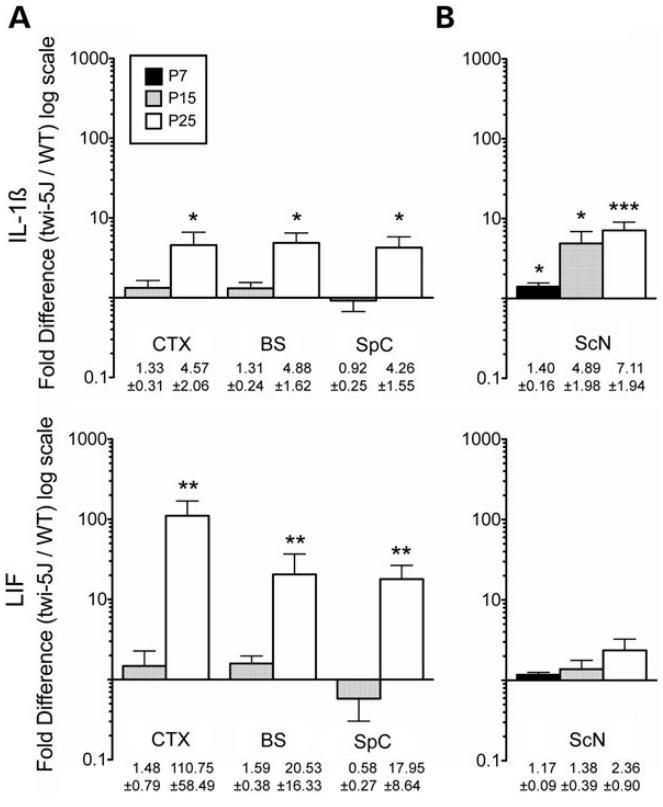

Figure 5. Inflammatory cytokine expression is increased in twi-5J nervous system. Quantitative RT–PCR for IL1-β and LIF expression was performed on RNA samples processed from the cortex (CTX), brainstem (BS), spinal cord (SpC) and sciatic nerve (ScN) of wild-type and twi-5J at P7, P15 or P25 (mean ± SEM, $n = 3$). (**A**) IL1-β and LIF expression is significantly increased in the CNS at P25, but not at P15. (**B**) In the sciatic nerve, IL1-β expression is significantly elevated and progressively increases starting at P7, while LIF expression is not increased in twi-5J compared with wild-type. $^{*}P < 0.05$; $^{**}P < 0.01$; $^{***}P < 0.005$.

revealed less myelinated large diameter axons in mutant sciatic nerve with an increase in g-ratio of 10 ± 0.05% for axons >2500 nm (Supplementary Material, Fig. S5A and B) in conjunction with a decrease in MBP isoforms (Supplementary Material, Fig. S4D). There was also evidence of an early inflammatory response in the nerve as indicated by few macrophages and elevated IL-1β gene expression (Fig. 5B, Supplementary Material, Fig. S5A). By P15, twi-5J sciatic nerve manifested significant edema, macrophage infiltration and marked elevation in IL-1β expression (Fig. 5B, Supplementary Material, Fig. S5C and D). These findings were accompanied by a shift in the composition of the myelinated axonal population toward smaller-diameter axons when compared with the wild-type, with a mean axonal diameter of 2151 versus 2471 nm, respectively ($P < 0.0001$). Concurrent normalization of g-ratios and MBP protein levels suggested axonal atrophy rather than myelin loss (Supplementary Material, Figs S4E and 5D). We did note an increase in the 17 kDa isoform as previously described in the twitcher sciatic nerve (27).

At the terminal stage of the disease (P23–P25), histological analysis demonstrated extensive hypomyelination in association with a 22 ± 2.3% decrease in axonal number that was attributable to a striking reduction among large diameter axons (Fig. 9E and F). Electron microscopy confirmed significant abnormalities in axons and myelination in twi-5J sciatic nerve around the time of demise (Fig. 9I–K). We observed redistribution in axon diameter with a profound loss of large diameter (>4000 nm) axons, along with their associated myelin sheaths (Fig. 8C). The wild-type sciatic nerve comprises 16% small, 62% medium, and 22% large diameter axons. In contrast, large diameter axons accounting for only 4% of the total axonal population in the twi-5J sciatic nerve, with small and medium diameter axons comprising 40 and 56%, respectively. The observed >80% loss among large diameter axons in twi-5J sciatic nerve correlated with the reduction in total axon number as assessed with toluidine blue. The overall decrease in myelinated axon caliber in twi-5J sciatic nerve was also reflected in a smaller mean diameter of 2344 vs. 3214 nm in the wild-type ($P < 0.0001$).

The remaining small (900–2000 nm) and medium (2000–4000 nm) caliber axons in the sciatic nerve showed perturbations in myelination. 7.2 ± 1.9 vs. 3.5 ± 0.6% of small diameter axons ($P < 0.05$) and 13.0 ± 1.06 vs. 4.7 ± 0.9% of medium diameter axons ($P < 0.01$) were hypomyelinated (g-ratio > 0.75) in the twi-5J vs. wild-type, respectively. Interestingly, a small and approximately equal percentage of the small and medium caliber axons had excess myelin wraps in relation to their size (g-ratio < 0.55) in the twi-5J compared with wild-type (Fig. 8C). The number of unmyelinated axons <900 nm was not significantly different between the twi-5J and wild-type and accounted for only 2% of the total axon population in the sciatic nerve.

The pathological changes in P25 twi-5J sciatic nerve were accompanied by worsening edema and inflammatory infiltrate, and progressive rise in IL-1β levels (Figs 5B and 9E–H). Interestingly, although we observed a gradual increase in LIF, it did not reach statistical significance even at P25 (Fig. 5B). Lipid inclusions were identified frequently in macrophages and more rarely within Schwann cells (Fig. 9J and K). We also noted slight perturbations in the Remak bundles, which appeared less compact in twi-5J than in the wild-type. The basal lamina of both myelinating and non-myelinating Schwann cells did not appear altered in twi-5J.

Psychosine concentrations are increased in twi-5J

The accumulation of psychosine (galactosylsphingosine), a by-product of GALC-enzymatic deficiency, is characteristic of Krabbe disease. Psychosine has been postulated to cause dysfunction of the nervous system through multiple mechanisms that are now beginning to be elucidated. Psychosine can trigger accumulation of macrophages, apoptosis, axonal degeneration via inhibition of lipid raft endocytosis, and may interfere with axon–glia signaling (28–30). As a neurotoxin, psychosine has been proposed to cause oligodendroglial cell death and demyelination. To test whether there was a correlation between psychosine accumulation and the neuropathological changes we observed in twi-5J, we measured the concentration of psychosine in cortex, brainstem, spinal cord and sciatic nerve samples of twi-5J and wild-type controls (Fig. 10). Psychosine concentrations were minimally increased in twi-5J at P15, but significantly elevated by P23 in both CNS and PNS (Fig. 10A and C). The highest levels of psychosine in twi-5J were measured

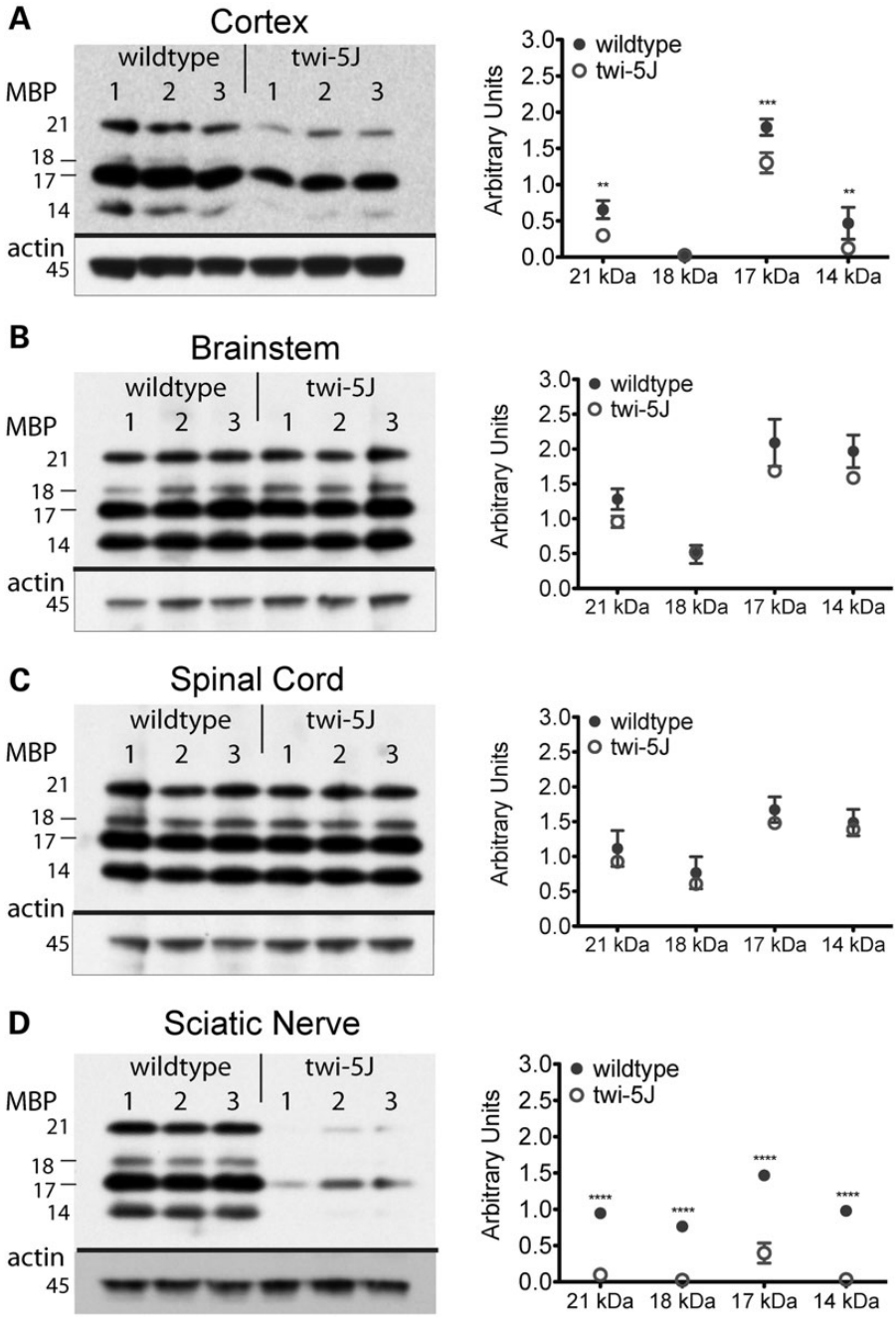

Figure 6. Expression of MBP isoforms is significantly decreased in twi-5J. Protein samples from three post-natal day 25 wild-type and twi-5J animals were separated by SDS–PAGE and examined for MBP expression by immunoblot analysis. MBP isoform expression was significantly decreased in the cortex (**A**) and sciatic nerve (**D**) of twi-5J. MBP expression within the brainstem and spinal cord were not significantly different. Each band is quantified relative to beta-actin expression and presented in arbitrary units. Data is plotted on the right as mean ± SD. $^{****}P < 0.0001$; $^{***}P < 0.001$; $^{**}P < 0.01$.

in the brainstem and spinal cord, where we observed gliosis and inflammatory cell infiltrates, but little disruption to axons or myelin. In contrast, psychosine levels were far lower in the forebrain and sciatic nerve, which manifested marked abnormalities in axons and myelin. Thus, psychosine levels in twi-5J do not correlate with nervous system regions exhibiting disturbances in myelination and axonopathy. Psychosine measurements in twitcher animals of comparable age (but different background strain) revealed 1.5–4-fold higher concentrations of this metabolite compared with twi-5J. Interestingly, the pattern of nervous tissue-specific psychosine accumulation in twitcher was similar to twi-5J, with the exception of the spinal cord which had relatively modest elevation compared with twitcher brainstem (Fig. 10B).

DISCUSSION

We have identified a missense mutation in mouse GALC, E130K, that causes a severe form of PNS dysmyelination and

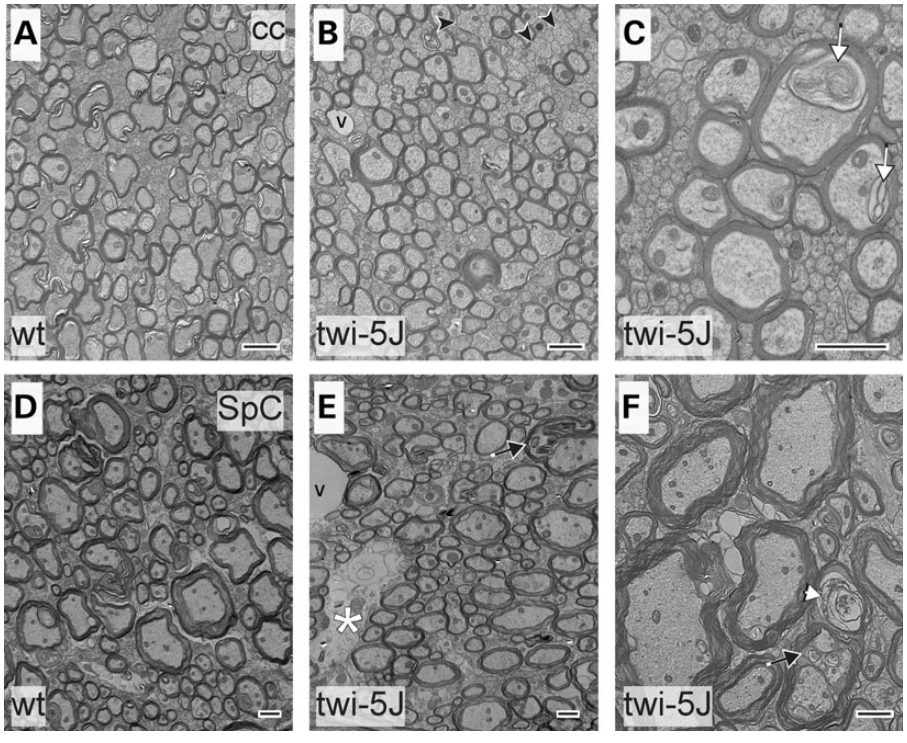

Figure 7. Electron microscopy of corpus callosum and spinal cord reveals ultrastructural abnormalities in twi-5J. Electron micrographs of the corpus callosum (cc) (**A**–**C**) and spinal cord (SpC) (**D**–**F**) post-natal day 25 wild-type (A and D) and twi-5J (B and C, E and F). Large diameter axons within the corpus callosum of twi-5J are normally myelinated. There is a small increase in unmyelinated medium-caliber axons (arrowheads) and lipid inclusions (white arrow, C). Spinal cord of twi-5J manifests occasional electron-light regions representing early signs of axonal loss (white asterisk), degenerating axons surrounded by compact myelin (white arrowhead) and lipid inclusions within axons (black arrow). v, blood vessel. Scale bar = 1 μm.

axonal loss, and demise during the fourth post-natal week. Twi-5J exhibit gliosis, globoid cells and psychosine accumulation without extensive perturbations in CNS myelination. A thorough comparison of twi-5J with twitcher based upon published studies is summarized in Figure 11. Unlike twitcher mice that contain a nonsense mutation that results in the loss of GALC protein, this missense mutation permits expression of a GALC precursor protein that is functionally impaired, resembling 25–45% of mutations found in Krabbe patients (7–9). Importantly, the *twi-5J* mutation has been identified in human patients with the infantile form of Krabbe disease (7,8), indicating that twi-5J is currently the only genetically authentic model of infantile Krabbe disease (9,31). In patients with the E130K substitution, GALC enzymatic activity was reported to be between 0 and 0.71% of average control values, similar to our findings in twi-5J. These patients exhibited disease onset by 5 months of age with death as early as 7 months (Mirella Filocamo, personal communication). The present findings included psychomotor arrest, hyperirritability, muscular hypotonia and decreased peripheral nerve conduction velocities (NCV) (8,32). Importantly, motor NCV were decreased in the upper and lower limbs, and sensory NCV were not detectable, indicative of severe PNS involvement (Mirella Filocamo, personal communication) (32). CNS hypomyelination was not reported among the MRI findings seen in these patients (8).

While the mechanism of how the E130K mutation affects GALC activity remains to be determined, studies of GALC missense mutations might offer insight. Three missense mutation, I1234T, D528N and L629R exhibit low enzymatic activity when exogenously expressed in a human CNS-derived cell line (10). All three mutations cause misprocessing of the GALC protein, impair lysosomal localization of the enzyme, and affect either the secretion or uptake of GALC protein. A therapeutic approach to treat lysosomal storage diseases involves using enzymatic inhibitors as ligands to protect newly synthesized, misfolded polypeptides from degradation. A weak inhibitor of GALC, α-lobeline, was shown to increase GALC activity of cells overexpressing the D528N mutation (10). Encouragingly, a recent structural analysis of GALC indicates the E130K mutation present in twi-5J may cause severe misfolding (33) such that similar types of small molecule pharmacological chaperones could improve $GALC^{E130K}$ activity and increase survival of twi-5J (10,34).

The mechanisms underlying nervous system pathology in Krabbe disease are still not completely understood. The 'psychosine hypothesis' proposed nearly 40 years ago to explain myelin loss observed in Krabbe disease suggested that psychosine, which accumulates due to GALC enzymatic deficiency, is responsible for rapid death of oligodendrocytes and demyelination (35,36). Psychosine accumulation is present in all twitcher animal models and is cytotoxic when applied *in vitro* or injected *in vivo* (37–39). Notably, the concentration of psychosine necessary to elicit a response in these studies is several orders of magnitude greater than documented *in vivo*, and a causative relationship between psychosine elevation and oligodendrocyte death has not been unequivocally established. Circumstantial

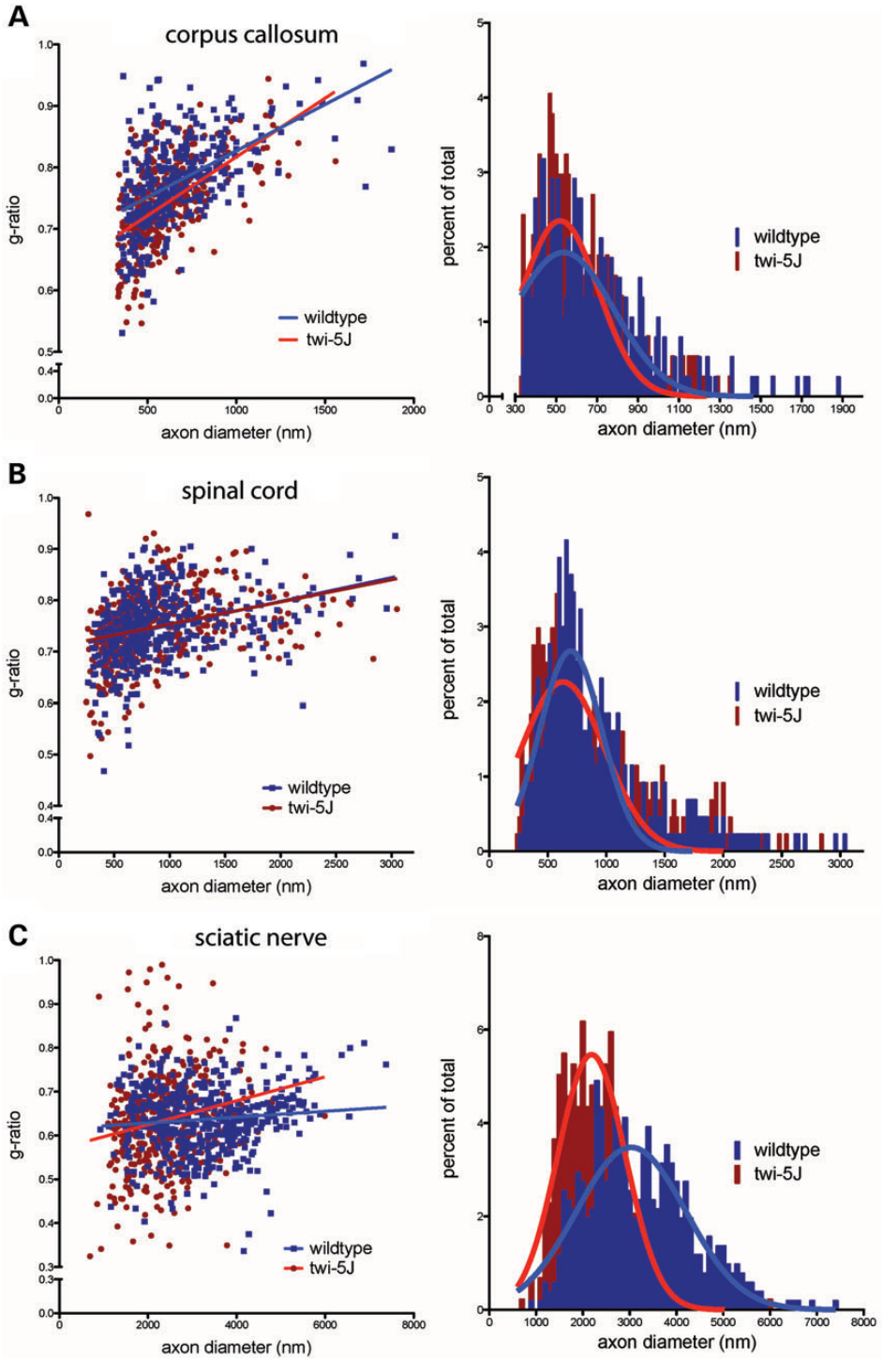

Figure 8. Analysis of myelinated axons reveals perturbations in axonal populations in twi-5J. G-ratio plot (left panels) and myelinated axon diameter distribution (right panels) for control and twi-5J in the corpus callosum (**A**), spinal cord (**B**) and sciatic nerve (**C**). (A) In the corpus callosum, a subset of small caliber axons (330–400 nm) are hypermyelinated and the number of large diameter axons (>650 nm) are reduced by ∼20% in twi-5J. (B) No significant changes in g-ratio or axon diameter are detected in the spinal cord. (C) Twi-5J exhibit loss of large axons (>4000 nm) and hypomyelination of small (900–2000 nm) and medium axons (2000–4000 nm). Significantly greater hyper-myelination of axons < 3000 nm in twi-5J offsets hypomyelination to generate averaged g-ratios comparable to wild-type at these axon diameters.

evidence that high levels of psychosine in the spinal cord and brainstem of twitcher correlate with regions most severely affected by the disease has been provided as *in vivo* evidence for the psychosine hypothesis (40). Our analysis reveals the remarkable finding that these regions of twi-5J CNS also manifest the highest psychosine concentrations, yet lack significant injury

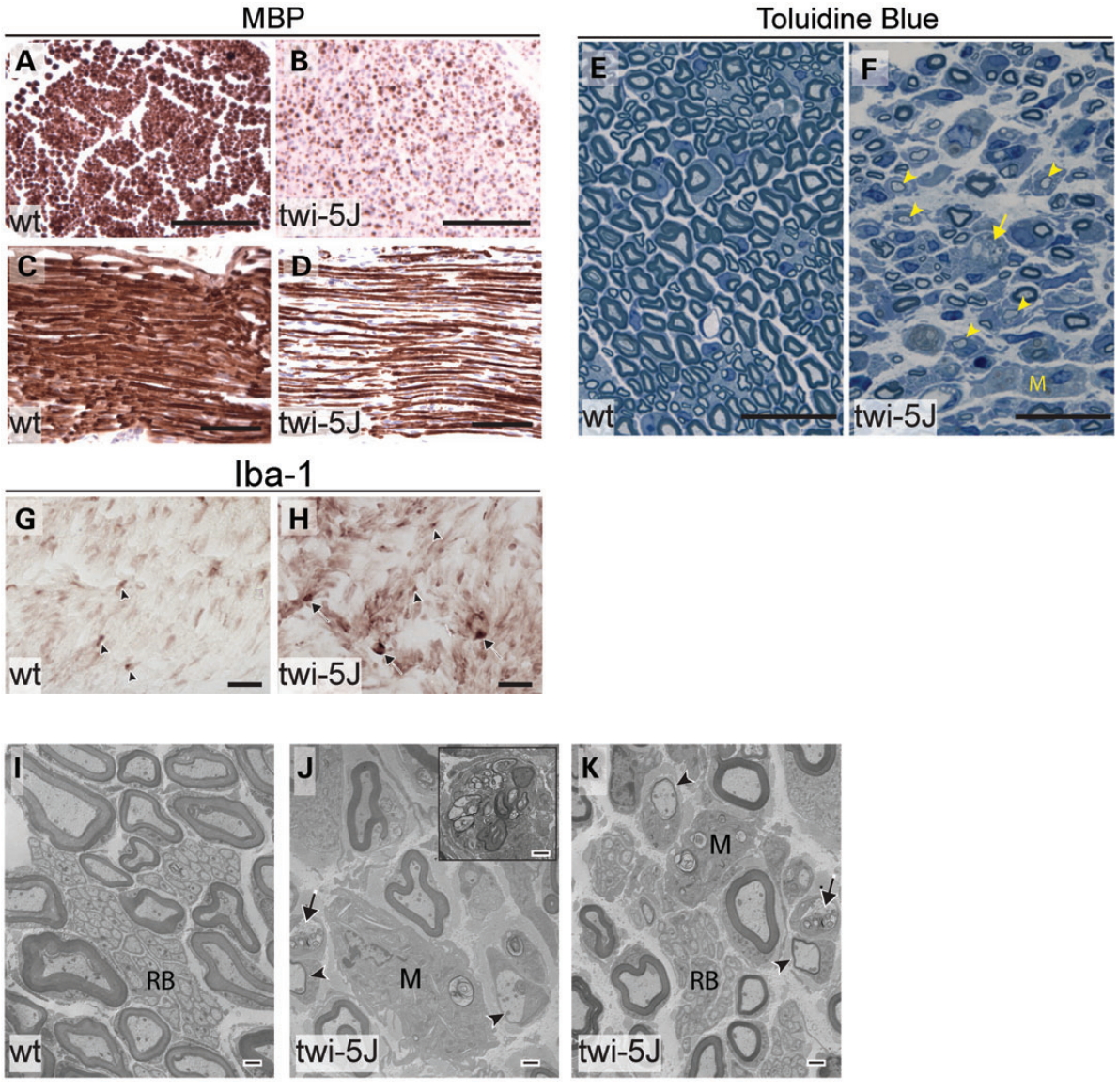

Figure 9. The sciatic nerves of twi-5J are severely hypomyelinated with macrophage accumulation. (**A**–**D**) MBP immunohistochemistry on cross-sections (A and B) and transverse-sections (C and D) through the sciatic nerve of P23 wild-type (A and C) and twi-5J (B and D) indicate significant myelin-deficiency in the PNS. (**E** and **F**) Toluidine blue staining on thin sections through the sciatic nerve of P25 wild-type control (E) and twi-5J (F). Compared with wild-type, the twi-5J sciatic nerve is less compact, exhibits ∼22% loss of axons and contain numerous hypomyelinated axons (arrowheads), macrophages (M) and large lipid-filled vesicles (arrows). (**G** and **H**) Iba-1 immunohistochemistry on cross-sections reveal accumulation of globoid cells (arrows) in twi-5J. Iba-1 also detects non-reactive macrophages in control and twi-5J sciatic nerve (arrowhead). (**I**–**K**) Electron microscopy of sciatic nerve of twi-5J reveals numerous macrophages, hypomyelinated axons and lipid inclusions compared with wild-type. Inset in J shows globoid cell. Black Arrows point to lipid inclusions. Arrowheads indicate hypomyelinated axons. M, macrophage; RB, Remak bundle. Scale bars: A–D = 250 μm; E–H = 25 μm; I–K = 1 μm.

to axons, myelin and oligodendroglia (Figs 4, 7, 8 and data not shown). In contrast, these pathological changes are present in regions with relatively low psychosine elevations. For example, axonal pathology and dysmyelination are apparent in the P15 twi-5J sciatic nerve with levels of psychosine similar to non-pathological concentrations present in wild-type samples at P25 (∼0.86 versus ∼2–3 pmol/mg protein). Extensive dysmyelination and axonal loss is present in the twi-5J sciatic nerve by P25, yet psychosine levels are substantially lower than measured or reported for twitcher at a comparable age (∼46 versus ∼158 pmol/mg protein) (41), underscoring the finding that axonal and myelin pathology do not correlate with tissue psychosine levels. This is consistent with the observation that psychosine is unable to induce Schwann cell death in twitcher animals *in vivo* (3,42). Like twitcher and twi-5J, infantile Krabbe patients exhibit higher levels of psychosine accumulation in the brainstem and spinal cord compared with the cortex (1,43). However, in contrast to twi-5J and twitcher, autopsy reports indicate psychosine levels in the human PNS may be higher than in CNS (43). These reports suggest differential psychosine accumulation between the mouse and human nervous system, and further implies that psychosine

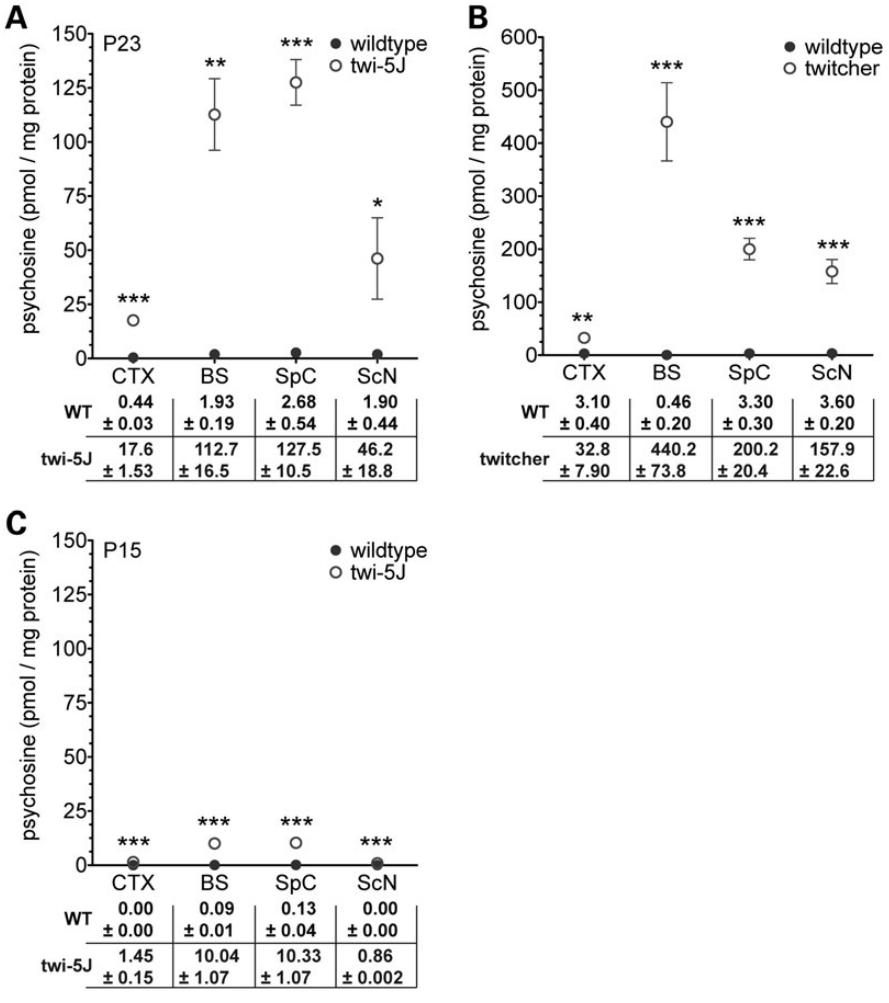

Figure 10. Psychosine levels are increased throughout the nervous system of twi-5J. (**A**) Psychosine concentrations (pmol/mg protein) were measured in tissue samples collected from cortex (CTX), brainstem (BS), spinal cord (SpC) and sciatic nerve (ScN) of post-natal day 23 twi-5J ($n = 3$) and wild-type littermates ($n = 3$). (**B**) Psychosine concentrations measured from P23–P25 twitcher and wild-type littermate tissue samples ($n = 3–5$). (**C**) Psychosine concentrations measured in tissue samples collected from cortex, brainstem, spinal cord and sciatic nerve of post-natal day 15 twi-5J ($n = 3$) and wild-type littermates ($n = 3$). Data plotted as mean ± SEM. $^{***}P < 0.001$; $^{**}P < 0.01$; $^{*}P < 0.05$.

concentrations do not adequately predict regions of greatest dysfunction. Furthermore, these data raise the possibility that psychosine or other metabolites of GALC disruption could differentially influence Schwann and oligodendrocyte function. Taken together, our results challenge the psychosine hypothesis and suggest that yet unknown mechanisms are responsible for axonal injury and eventual myelin loss.

Our data further argue that widespread CNS demyelination is not the principal or most critical mechanism in the pathogenesis or early death in some forms of infantile Krabbe disease. Indeed, peripheral neuropathy is among the presenting manifestations in the most severe forms of Krabbe disease (44). Similarly, the earliest pathological changes in twi-5J appear in the sciatic nerve at P7 and preferentially affect large caliber axons, progressing to severe axonal and myelin loss at terminal stages of the disease. The reduction in myelin in twi-5J sciatic nerve is associated with, and likely a consequence of, the preferential loss of large caliber, heavily myelinated axons. Consistent with these findings, recent studies in the twitcher also show axonal pathology at P7, a week prior to initial signs of demyelination, suggesting that Schwann cell dysfunction and myelin loss could be secondary to axonal injury in the pathogenesis of Krabbe disease (28,29). However, there is conflicting evidence as to axonal loss in the twitcher sciatic nerve, but it appears to be a relatively late outcome confined to the peroneal nerve (3,4,41,45).

We predict that axonal and myelin loss observed in the twi-5J sciatic nerve likely reflect widespread axonopathy and hypomyelination throughout the peripheral nervous system, including the enteric and autonomic nerves that could account for the early lethality of twi-5J at ~23 days. In support of this hypothesis, we observed cranial nerve edema and sudden death in twi-5J animals suggestive of autonomic dysregulation such as an arrhythmia (data not shown). Krabbe patients with E130K mutation manifest signs of autonomic dysfunction including bradycardia and dysphagia, as well as multiple cranial nerve enhancements on MRI (Mirella Filocamo, personal communication). Understanding why twi-5J die sooner than twitcher will be

A

Allele	*twi*	*twi*	*twi*	*trs, tm1Wngr*	*twi-5J*
Genetic Background	B6;CE	B6;FVB	B6.CE	129S2/SvPas	BXD32/Ty
Mutation	1017G>A, W332X			502-503 CA>TG, H168C	388G>A, E130K
Onset of clinical symptoms (day)	~30	~21	~15	~25	~15
Age of Death (days)	~90	~50	~43	~58	~23
Head & generalized tremors	Yes	Yes	Yes	Yes	Yes
Decreased body weight	Yes	Yes	Yes	Yes, delayed	Yes
Muscle weakness and hindlimb wasting	Yes	Yes	Yes	Yes	Yes, mild
Progressive hindlimb paralysis	Yes	Yes	Yes	Yes	Yes
Selected References:	(1, 2)	(46. 56-58)	(29, 37, 41, 48, 59, 60)	(17, 47, 61)	this report and (51)

B6;CE = mixed C57BL/6J with CE/J. B6; FVB = mixed C57Bl/6J with FVB. B6.CE = C57BL/6J congenic strain

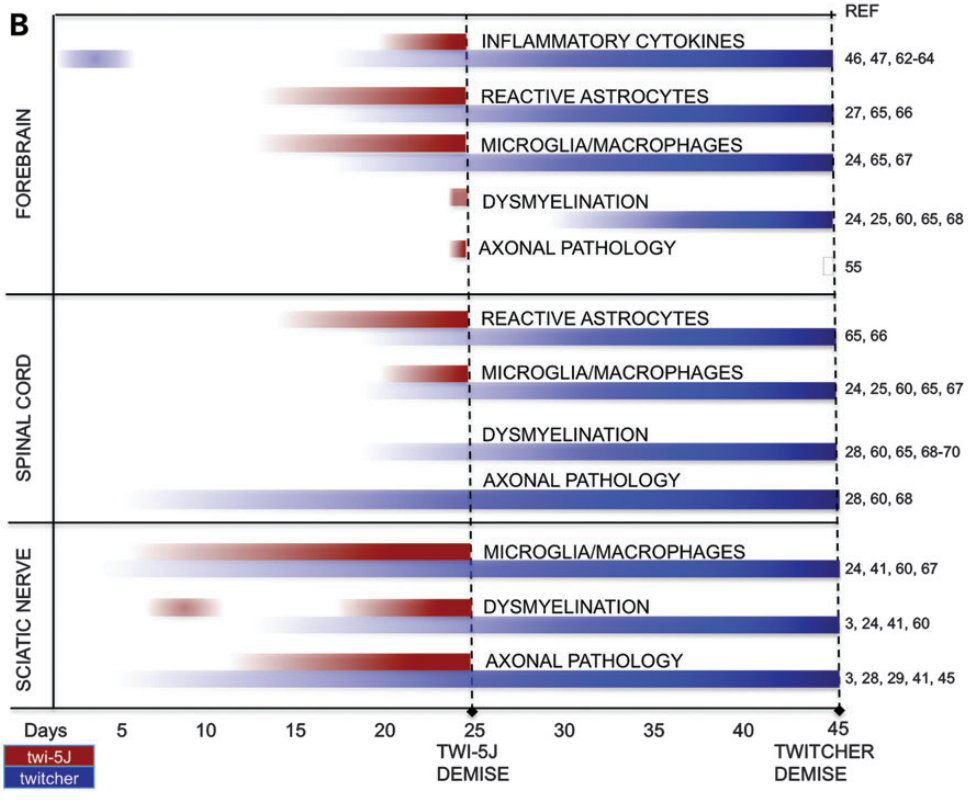

Figure 11. Comparison of twi-5J and twitcher clinical symptoms and disease progression. (**A**) Clinical symptoms of Krabbe disease mouse models. (**B**) Schematic comparing characteristics of disease progression between twi-5J and twitcher in the CNS and PNS. In the forebrain, axonal pathology is observed in twi-5J but not in twitcher. In contrast, significant axonal pathology is not detected in the spinal cord of twi-5J. The twi-5J sciatic nerve exhibits early perturbation in myelination, normalization of g-ratios and MBP expression by P15, and severe dysmyelination by P25. Inflammatory cytokine progression in the spinal cord and sciatic nerve has not been examined in twitcher (56,70). A comparison of psychosine accumulation is presented in Figure 10.

an important avenue for future studies and could provide insight into GALC function and the pathogenesis of different forms of Krabbe disease.

Our data are consistent with recent observations in twitcher indicating the presence of CNS inflammation early in the course of disease progression and preceding onset of demyelination (46,47). The presence of large macrophages in the forebrain and spinal cord of twi-5J is also consistent with globoid cell accumulation in Krabbe patients (25). Widespread CNS inflammation and gliosis without significant demyelination at the terminal stage of disease in twi-5J indicates that CNS myelin loss may be secondary and relatively late event in disease progression and not the primary mechanism for macrophage activation and accumulation as previously hypothesized (48). Recent observations in twitcher brain show the elevation of several pro-inflammatory cytokines including Tnfa, Ccl2 and Cxcl10

at P2 and P20, but not P10, suggesting an unexplained biphasic regulation of inflammation in the CNS in advance of demyelination (46,47). With our analysis, we sought to extend these findings by examining both pro- and anti-inflammatory cytokines in various regions of the nervous system as they correlate with neuropathology. Although IL-1β has detrimental effects on cell viability, LIF has been reported as protective of neuron and oligodendrocytes in a demyelinating disease mouse model (49,50). While IL-1β was significantly elevated in both CNS and PNS of twi-5J by P25, only the CNS had a significant and robust increase in LIF expression. Correspondingly, the CNS showed relative preservation of axons and myelin when compared with the PNS. These data suggest the intriguing possibility that competing cytokine action in immune regulation could determine severity of axonopathy and myelin loss in Krabbe disease. Our findings further support the notion that CNS inflammation may play a critical role in disease progression independent of myelin loss (46,50).

Our identification of the causative mutation in *twi-5J* should be useful in uncovering the molecular mechanisms underlying a subset of infantile forms of Krabbe disease. The disparity between psychosine levels and demyelination in twi-5J challenges the longstanding concept that elevated levels of psychosine underlie the pathophysiological progression of Krabbe disease. Twi-5J could become an important mouse model of Krabbe disease for evaluating the effectiveness of therapeutics, such as stem cell or glial transplantation, gene therapy or drug screening.

MATERIALS AND METHODS

Mice

All procedures at JAX, UCSF or OHSU were approved by Institutional Animal Care and Use Committees (JAX comprehensive protocol #99066; UCSF protocol number AN081844; OHSU protocol number IS1153). The mutant strain (BXD32/TyJ-*Galc*$^{twi\text{-}5J}$, twitcher 5 Jackson, referred to as twi-5J) is available from JAX (Stock Number: JR003613).

Immunohistochemistry

Twi-5J and control littermate mice were perfused with phosphate buffered saline followed by 4% paraformaldehyde; tissues were dissected out, and forebrain and brainstem sectioned at 50 μm on a Leica Vibratome and spinal cord and sciatic nerves were cryopreserved in O.C.T. compound (and sectioned at 20 μm on a Leica Cryostat. Antibodies used were: anti-GFAP (anti-rabbit, Chemicon), anti-MBP (anti-rat MBP, Millipore) or anti-Iba-1 (anti-rabbit, Wako Pure Chemicals). We examined histopathology at ages 7 days (three twi-5J, 1 heterozygote, three wild-type), P15 (three twi-5J, three wild-type), P21–P25 (nine twi-5J, nine wild-type controls).

Electron microscopy

Twi-5J and wild-type littermates ($n = 3$ for each) were perfused at P7, P15 and P25 with 0.1 M phosphate buffer followed by 2.0% paraformaldehyde/2.5% glutaraldehyde in 0.1 M phosphate buffer. The brain, spinal cord, brainstem and sciatic nerves were isolated, and 1 mm blocks were post-fixed in 1.5% glutaraldehyde/1.5% paraformaldehyde in 0.1 M Sodium cacodylate buffer, pH 7.4 with 0.05 M sucrose and 0.25% $CaCl_2$ for 160 min. Tissue was then processed for EM in a Pelco BioWave through a series of solutions including sodium cacodylate buffer, osmium tetroxide and uranyl acetate before embedding in spur:epon. 700 nm sections were cut and stained with toluidine blue to evaluate tissue integrity and orientation. Ultrathin (70 nm) sections were then cut and counterstained with uranyl acetate and lead citrate. EM images were captured on a FEI Technai G2 12 Biotwin at 80 kV. Quantification of axon numbers and size between three wild-type and twi-5J age-matched pairs was performed on digital EM or toluidine blue images using ImageJ. Mean size, axonal distribution and Gaussian curves were calculated using Prism5 (GraphPad Software, Inc.). A total of 8720 myelinated axons were counted from toluidine blue-stained sciatic nerves. 762, 1161, 1158 nerves were quantified on corpus callosum, spinal cord and sciatic nerve EM digital images, respectively. Statistical significance was tested using the unpaired *t*-test, Fisher's exact *t*-test or the unpaired *t*-test with Welch's correction where appropriate.

twi-5J mutation identification

For genetic mapping of the new mutation, ovaries from twi-5J females were transplanted into histocompatible hosts and bred to CAST/EiJ males; the obligate heterozygous F1s were intercrossed and affected F2 progeny genotyped by PCR for DNA markers on all chromosomes. Genotyping DNA from affected progeny showed that the mutation was located on Chromosome 12 between *D12Mit6* and *D12Mit262* (51). As the twitcher mutation is located in this region, we performed a direct genetic non-complementation test with the original twitcher mutation. A heterozygous *twi-5J* male was mated to a heterozygous twitcher female producing 15 offspring in 2 l, of which five progeny exhibited the twitcher phenotype indicating that *twi-5J* is a twitcher allele.

Heterozygous *twi-5J* mice were bred to produce twi-5J offspring and unaffected mice. By 18 days of age, twi-5J are distinguishable from unaffected mice by body size and tremors. Genomic DNA was isolated from tail-tip biopsies of control and twi-5J mice, and the GALC exons were sequenced by the Genomic Core Facility at UCSF. One non-synonymous variation was identified in exon 4 of twi-5J animals.

Allele specific-PCR genotyping

To genotype the *twi-5J* animals, we developed an allele-specific PCR strategy based on an amplification refractory mutation system (52). Allele-specific primers were designed using the BatchPrimer3 program and produce a PCR product ∼160 bp (53). GALC-388G: 5′-CTT CTT AGC TTC CTT CAT TAG CCA CCA CGC-3′; GALC-388A: 5′-CTT CTT AGC TTC CTT CAT TAG CCA CCA CGT-3′; Common primer: 5′-GTG CAT GTG TGT GTA CTT AAG AGG CTC TGG-3′.

Site-directed mutagenesis

Full-length mouse *Galc* coding sequence was isolated by PCR from pYX-Asc GALC purchased from Open Biosystems

(clone # 30635559) and cloned into Gateway entry vector pENTR 3C. The pENTR-mGALC plasmid was sequenced to confirm no errors. To generate the G to A nucleotide change at nucleotide 388, the QuickChange Lightning kit was used according to manufacturer guidelines (Invitrogen). Primers: GALC-G388A sense: 5′-CTA GAT GAG AAT TAT TTC CGA GGC TAT **A**AG TGG TGG CTA ATG-3′; GALC-G388A antisense: 5′-CAT TAG CCA CCA CT**T** ATA GCC TCG GAA ATA ATT CTC ATC TAG-3′. The twi-5J nucleotide is emphasized. The pENTR-mGALC-E130K plasmid was sequenced to confirm only the expected nucleotide was changed. Both pENTR-mGALC and pENTR-mGALC-E130K were transferred into a mammalian expression Gateway destination (pCMV-myctag-Dest) vector using LR Clonase II (Invitrogen).

GALC activity

Histochemistry

COS-7 cells were transiently transfected using Fugene6 (Promega) with expression constructs for GFP (to control for transfection efficiency) and GALC or GALC-G388A. Forty-eight hours after transfection, the cells were fixed with 2% PFA and a modified X-Gal histochemistry for GALC enzymatic activity was performed as described (18). Cells were washed 3x with PBS, equilibrated for 15 min in 50 mM citrate/phosphate buffer (pH 4.0) and then equilibrated 15 min in 5 mg/ml taurodeoxycholic acid and 5 mg/ml oleic acid in citrate/phosphate buffer. Cells were incubated for 2 h in 2 mg/ml X-Gal staining solution containing 5 mg/ml taurodeoxycholic acid, 5 mg/ml oleic acid and 5 mM potassium ferrocyanide and ferricyanide in citrate/phosphate buffer at 37°C. The reaction was stopped by washing the cells 3x in PBS before mounting onto glass slides using CC mount. Expression of GALC and GALC-E130K was verified by western blot.

Cellular activity

To quantify cellular GALC enzymatic activity from cell or brain extracts, we used a previously described assay (19). Cells were harvested in ice cold PBS, centrifuged at 300*g*, washed in PBS, and pelleted by centrifugation at 13 400*g*. Cell pellets were stored at −80°C until processed for GALC activity. Cell pellets were suspended in ice cold 10 mM sodium phosphate buffer pH 6.0 (1 × 10 cm plate of cells/1.5 ml buffer), containing 0.1% (vol/vol) Nonidet NP-40, and subjected to sonication of 3 × 15 s pulses at 18 W, followed by incubation for 1 h at 4°C. For brain extracts, control and twi-5J animals were euthanized by CO_2 asphyxiation according to IACUC guidelines. The brains were dissected from the skull and then hemisected. Each hemisphere was flash frozen on liquid nitrogen and then stored at −80°C until processed for GALC activity. Tissues were homogenized with an Elveheim type homogenizer in 10 mM sodium phosphate buffer pH 6.0 (∼5 mg tissue/mL buffer) with 0.1% (vol/vol) Nonidet NP-40 and then subjected to three rounds of sonication. After 1 h on ice, brain lysates were aliquoted into Eppendorf microcentrifuge tubes and centrifuged at 13 400*g* for 10 min. We used supernatants as tissue extracts for biochemical analyses. All procedures were carried out at 4°C. We measured protein content of cell and brain extracts using the Bio-Rad Bradford Protein Assay kit with bovine serum albumin as the reference standard.

We performed the GALC enzymatic assay by mixing 15 μg protein extract with 100 μl of reaction solution containing 1.5 mM 4-methylumbelliferone-β-galactopyranoside (MUGAL, Sigma, M1633) substrate and 11 μM $AgNO_3$ resuspended in 0.1 M citrate/0.2 M phosphate buffer, pH 4.0. Reactions were incubated 30 min at 37°C and then stopped with 0.2 M glycine/NaOH, pH 10.6. We measured fluorescence (IF) of liberated 4-methylumbelliferone (4-MU) using a SpectraMax M2 spectrofluorometer (λ_{ex} 365 nm, λ_{em} 445 nm). Activity (nmols/min) was calculated as: IF of sample * f * final sample dilution ÷ time (min). f is calculated from a standard 4-MU (Sigma, M1381) curve equal to [4-MU]/IF MU. All assays were done in triplicate using three independent samples and reported as mean ± SD. Significance between experimental groups was calculated using ANOVA or Student's t-test using GraphPad Prism 4.0.

Measurement of psychosine concentration

The cortical hemispheres, spinal cord, brainstem (not including midbrain) and sciatic nerves of three twi-5J and three wild-type littermates at P15 and P23 were isolated and snap frozen on dry ice. Tissues were homogenized in cold water using a Polytron homogenizer (IKA T8.10, Werke) (cerebrum and brainstem) or disaggregated by ultrasound (10 s intervals, Sonics Vibra Cell) (cords and nerves). Protein concentration was determined using the Bradford Assay. Homogenates were extracted with 2 ml chloroform–methanol (2:1), filtered and dried under nitrogen in a 42°C water bath. Dried extracts were re-suspended in 2 ml of methanol and applied to activated LC-SCX SPE columns for solid phase extraction (Supelco, PA, USA). Columns were rinsed as described (54). Lipids were released by elution with methanol:0.4 M calcium chloride (3:1). Eluates were applied to C18 Bond Elut columns (Agilent Technologies). Psychosine was eluted with 7.5 ml of chloroform–methanol 1:2, dried and re-suspended in methanol containing 5 mM ammonium formate. Lyso-lactosylceramide (Matreya, PA, USA) was added as internal reference to all samples prior to extraction. Psychosine was quantified by HPLC tandem mass spectrometry (LC/MS/MS). Samples were first passed through a Shimadzu Shimpak VP-ODS-C18 reverse phase 4.5 × 150 mm for HPLC, followed by triple quadrupole mass spectrometry with a Shimadzu LCMS-8030 spectrometer. Analyte concentrations were normalized to protein concentration.

Quantitative PCR

Total RNA was isolated from flash frozen P7, P15 and P25 wild-type and twi-5 tissue ($n = 3$ each) using the RNeasy Mini Lipid Kit (Qiagen) and converted to cDNA using the Taqman Reverse Transcription reagent (Applied Biosystems). Quantitative PCR for LIF1 and IL-1β was performed using Taqman probes Mm00434761_m1 for LIF1 and Mm01336189_m1 for IL-1β as described (55). The average dCt was computed for each sample relative to endogenous 18S, and the relative quantity of LIF1 and IL-1β gene expression was calculated from the dCt. The fold change in relative quantity of LIF1 and IL-1β expression was calculated as the ratio of relative quantity between twi-5J to wild-type.

Western blot

Brain and cell extracts were separated by SDS–PAGE and transferred to BioTrace PVDF membrane (Pall Life Sciences), immunoblotted with GALC antibody (CL1021AP, 1:1000, chicken anti-GALC provided by Chris and Elizabeth Eckman, Atlantic Neonatal Research Institute) (10) or rat anti-MBP (Millipore, 1:3000) and detected using ECL (Amersham Biosciences). After detection, blots were extensively washed and blotted with mouse anti-beta-actin (Chemicon MAB3408, 1:10 000). Blots were digitized using a FujiFilm LAS-4000 and quantified using ImageJ. Samples from three independent sets of experiments were standardized to beta-actin and averaged. Significance ($P < 0.05$) between experimental groups was calculated using unpaired, two-tailed *t*-test or ANOVA by GraphPad Prism5.

SUPPLEMENTARY MATERIAL

Supplementary Material is available at *HMG* online.

ACKNOWLEDGEMENTS

We would like to thank Jon Woo at the Genome Core Facility at UCSF for help with GALC-exome sequencing, Mirella Filocamo of the Giannina Gaslini Institute (Genova, Italy) for communication of unpublished Krabbe patient records, Jordan Ward and Simon Boulton for the pCMV-myctag-Dest vector, Jon Zweig for assistance with immunohistochemistry, E. Belle Borovik and Thuy Luu for help with mouse maintenance, Christopher and Elizabeth Eckman for sharing the chicken anti-GALC antibody, Paul Barnes for western blot reagents and gift of the beta-actin antibody, Robert Kayton and Lisa Vecchiarelli at the Immuno Electron Microscopy Core at OHSU, Pete Levasseur for cytokine qPCR, Martha Buzzell and Benjamin Taylor for identifying the twi-5J mutants and transferring them to the Mouse Mutant Resource, Son Yong Karst and Patricia Ward-Bailey for genetic analysis of twi-5J and The Jackson Laboratory Histopathology Sciences personnel for making histological preparations and immunohistochemistry. We thank Dan Marks, Markus Grompe, Vivek Unni, Chris Potter and Bob Steiner for critical comments on the manuscript.

Conflict of Interest statement. None declared.

FUNDING

This work was supported by the National Institutes of Health (NS040511 to D.H.R., K08-NS062744 to M.A.P.; P40 RR001183 to M.T.D.; P30 NS061800 ‘Neuroscience Imaging Center at OHSU’ to Sue A. Aicher); Department of Human and Health Services (RNS065808A to E.R.B.); European Leukodystrophies Association Foundation (ELA 2010-036F34 to G.B.P.); Pollin Pediatric Research Prize, and a private donation from the Kinnune family to M.A.P.; and The Jackson Laboratory’s Cancer Center Core Grant (CA34196). D.H.R. is an HHMI Investigator.

REFERENCES

1. Igisu, H. and Suzuki, K. (1984) Progressive accumulation of toxic metabolite in a genetic leukodystrophy. *Science*, **224**, 753–755.
2. Xu, Y.H., Barnes, S., Sun, Y. and Grabowski, G.A. (2010) Multi-system disorders of glycosphingolipid and ganglioside metabolism. *J. Lipid Res.*, **51**, 1643–1675.
3. Jacobs, J.M., Scaravilli, F. and De Aranda, F.T. (1982) The pathogenesis of globoid cell leucodystrophy in peripheral nerve of the mouse mutant twitcher. *J. Neurol. Sci.*, **55**, 285–304.
4. Suzuki, K. and Taniike, M. (1995) Murine model of genetic demyelinating disease: the twitcher mouse. *Microsc. Res. Tech.*, **32**, 204–214.
5. Wenger, D.A. (1997) Krabbe disease. GeneReviews at GeneTests: Medical Genetics Information Resource (database online). Copyright, University of Washington, Seattle, 2010.
6. Rafi, M.A., Luzi, P., Chen, Y.Q. and Wenger, D.A. (1995) A large deletion together with a point mutation in the GALC gene is a common mutant allele in patients with infantile Krabbe disease. *Hum. Mol. Genet.*, **4**, 1285–1289.
7. Lissens, W., Arena, A., Seneca, S., Rafi, M., Sorge, G., Liebaers, I., Wenger, D. and Fiumara, A. (2007) A single mutation in the GALC gene is responsible for the majority of late onset Krabbe disease patients in the Catania (Sicily, Italy) region. *Hum. Mutat.*, **28**, 742.
8. Tappino, B., Biancheri, R., Mort, M., Regis, S., Corsolini, F., Rossi, A., Stroppiano, M., Lualdi, S., Fiumara, A., Bembi, B. *et al.* (2010) Identification and characterization of 15 novel GALC gene mutations causing Krabbe disease. *Hum. Mutat.*, **31**, E1894–E1914.
9. Duffner, P.K., Barczykowski, A., Jalal, K., Yan, L., Kay, D.M. and Carter, R.L. (2011) Early infantile Krabbe disease: results of the World-Wide Krabbe Registry. *Ped. Neurol.*, **45**, 141–148.
10. Lee, W.C., Kang, D., Causevic, E., Herdt, A.R., Eckman, E.A. and Eckman, C.B. (2010) Molecular Characterization of mutations that cause globoid cell leukodystrophy and pharmacological rescue using small molecule chemical chaperones. *J. Neurosci.*, **30**, 5489–5497.
11. Wenger, D.A., Rafi, M.A. and Luzi, P. (1997) Molecular genetics of Krabbe disease (globoid cell leukodystrophy): diagnostic and clinical implications. *Hum. Mutat.*, **10**, 268–279.
12. Duffner, P.K., Caggana, M., Orsini, J.J., Wenger, D.A., Patterson, M.C., Crosley, C.J., Kurtzberg, J., Arnold, G.L., Escolar, M.L., Adams, D.J. *et al.* (2009) Newborn screening for Krabbe disease: the New York State model. *Ped. Neurol.*, **40**, 245–252.
13. Sakai, N., Inui, K., Tatsumi, N., Fukushima, H., Nishigaki, T., Taniike, M., Nishimoto, J., Tsukamoto, H., Yanagihara, I., Ozono, K. *et al.* (1996) Molecular cloning and expression of cDNA for murine galactocerebrosidase and mutation analysis of the twitcher mouse, a model of Krabbe’s disease. *J. Neurochem.*, **66**, 1118–1124.
14. Lee, W.C., Tsoi, Y.K., Dickey, C.A., DeLucia, M.W., Dickson, D.W. and Eckman, C.B. (2006) Suppression of galactosylceramidase (GALC) expression in the twitcher mouse model of globoid cell leukodystrophy (GLD) is caused by nonsense-mediated mRNA decay (NMD). *Neurobiol. Disease*, **23**, 273–280.
15. Duchen, L.W., Eicher, E.M., Jacobs, J.M., Scaravilli, F. and Teixeira, F. (1980) Hereditary leucodystrophy in the mouse: the new mutant twitcher. *Brain*, **103**, 695–710.
16. Kobayashi, T., Yamanaka, T., Jacobs, J.M., Teixeira, F. and Suzuki, K. (1980) The Twitcher mouse: an enzymatically authentic model of human globoid cell leukodystrophy (Krabbe disease). *Brain Res.*, **202**, 479–483.
17. Luzi, P., Rafi, M.A., Zaka, M., Curtis, M., Vanier, M.T. and Wenger, D.A. (2001) Generation of a mouse with low galactocerebrosidase activity by gene targeting: a new model of globoid cell leukodystrophy (Krabbe disease). *Mol. Genet. Metab.*, **73**, 211–223.
18. Dolcetta, D., Perani, L., Givogri, M.I., Galbiati, F., Orlacchio, A., Martino, S., Roncarolo, M.G. and Bongarzone, E. (2004) Analysis of galactocerebrosidase activity in the mouse brain by a new histological staining method. *J. Neurosci. Res.*, **77**, 462–464.
19. Martino, S., Tiribuzi, R., Tortori, A., Conti, D., Visigalli, I., Lattanzi, A., Biffi, A., Gritti, A. and Orlacchio, A. (2009) Specific determination of -galactocerebrosidase activity via competitive inhibition of -galactosidase. *Clin. Chem.*, **55**, 541–548.
20. Chen, Y.Q., Rafi, M.A., de Gala, G. and Wenger, D.A. (1993) Cloning and expression of cDNA encoding human galactocerebrosidase, the enzyme deficient in globoid cell leukodystrophy. *Hum. Mol. Genet.*, **2**, 1841–1845.

21. Nagano, S., Yamada, T., Shinnoh, N., Furuya, H., Taniwaki, T. and Kira, J. (1998) Expression and processing of recombinant human galactosylceramidase. *Clin. Chim. Acta*, **276**, 53–61.
22. Strazza, M., Luddi, A., Carbone, M., Rafi, M.A., Costantino-Ceccarini, E. and Wenger, D.A. (2009) Significant correction of pathology in brains of twitcher mice following injection of genetically modified mouse neural progenitor cells. *Mol. Genet. Metab.*, **97**, 27–34.
23. Suzuki, K. (2003) Globoid cell leukodystrophy (Krabbe's disease): update. *J. Child Neurol.*, **18**, 595–603.
24. Ohno, M., Komiyama, A., Martin, P.M. and Suzuki, K. (1993) Proliferation of microglia/macrophages in the demyelinating CNS and PNS of twitcher mouse. *Brain Res.*, **602**, 268–274.
25. Takahashi, H., Igisu, H. and Suzuki, K. (1983) The twitcher mouse: an ultrastructural study on the oligodendroglia. *Acta Neuropath.*, **59**, 159–166.
26. Siddiqi, Z.A., Sanders, D.B. and Massey, J.M. (2006) Peripheral neuropathy in Krabbe disease: electrodiagnostic findings. *Neurology*, **67**, 263–267.
27. Mikoshiba, K., Fujishiro, M., Kohsaka, S., Okano, H., Takamatsu, K. and Tsukada, Y. (1985) Disorders in myelination in the twitcher mutant: immunohistochemical and biochemical studies. *Neurochem. Res.*, **10**, 1129–1141.
28. Castelvetri, L.C., Givogri, M.I., Zhu, H., Smith, B., Lopez-Rosas, A., Qiu, X., van Breemen, R. and Bongarzone, E.R. (2011) Axonopathy is a compounding factor in the pathogenesis of Krabbe disease. *Acta Neuropath.*, **122**, 35–48.
29. Smith, B., Galbiati, F., Castelvetri, L.C., Givogri, M.I., Lopez-Rosas, A. and Bongarzone, E.R. (2011) Peripheral neuropathy in the Twitcher mouse involves the activation of axonal caspase 3. *ASN Neuro.*, **3**, 213–222.
30. White, A.B., Galbiati, F., Givogri, M.I., Lopez Rosas, A., Qiu, X., van Breemen, R. and Bongarzone, E.R. (2011) Persistence of psychosine in brain lipid rafts is a limiting factor in the therapeutic recovery of a mouse model for Krabbe disease. *J. Neurosci. Res.*, **89**, 352–364.
31. Stenson, P.D., Mort, M., Ball, E.V., Howells, K., Phillips, A.D., Thomas, N.S. and Cooper, D.N. (2009) The Human Gene Mutation Database: 2008 update. *Genome Med.*, **1**, 13.
32. Morana, G., Biancheri, R., Dirocco, M., Filocamo, M., Marazzi, M.G., Pessagno, A. and Rossi, A. (2009) Enhancing cranial nerves and cauda equina: an emerging magnetic resonance imaging pattern in metachromatic leukodystrophy and krabbe disease. *Neuropediatrics*, **40**, 291–294.
33. Deane, J.E., Graham, S.C., Kim, N.N., Stein, P.E., McNair, R., Cachon-Gonzalez, M.B., Cox, T.M. and Read, R.J. (2011) Insights into Krabbe disease from structures of galactocerebrosidase. *Proc. Natl Acad. Sci. USA*, **108**, 15169–15173.
34. Valenzano, K.J., Khanna, R., Powe, A.C., Boyd, R., Lee, G., Flanagan, J.J. and Benjamin, E.R. (2011) Identification and characterization of pharmacological chaperones to correct enzyme deficiencies in lysosomal storage disorders. *Assay Drug Dev. Technol.*, **9**, 213–235.
35. Suzuki, K. (1998) Twenty five years of the "psychosine hypothesis": a personal perspective of its history and present status. *Neurochem. Res.,* **23**, 251–259.
36. Miyatake, T. and Suzuki, K. (1972) Globoid cell leukodystrophy: additional deficiency of psychosine galactosidase. *Biochem. Biophys. Res. Commun.*, **48**, 539–543.
37. LeVine, S.M., Wetzel, D.L. and Eilert, A.J. (1994) Neuropathology of twitcher mice: examination by histochemistry, immunohistochemistry, lectin histochemistry and Fourier transform infrared microspectroscopy. *Int. J. Dev. Neurosci.*, **12**, 275–288.
38. Giri, S., Khan, M., Rattan, R., Singh, I. and Singh, A.K. (2006) Krabbe disease: psychosine-mediated activation of phospholipase A2 in oligodendrocyte cell death. *J. Lipid Res.*, **47**, 1478–1492.
39. Suzuki, K. and Tanaka, H. (1976) Studies on the pathogenesis of Krabbe's leukodystrophy: cellular reaction of the brain to exogenous galactosylsphingosine, monogalactosyl diglyceride, and lactosylceramide. *Adv. Exp. Med. Biol.*, **68**, 99–114.
40. Shinoda, H., Kobayashi, T., Katayama, M., Goto, I. and Nagara, H. (1987) Accumulation of galactosylsphingosine (psychosine) in the twitcher mouse: determination by HPLC. *J. Neurochem.*, **49**, 92–99.
41. Tanaka, K., Nagara, H., Kobayashi, T. and Goto, I. (1988) The twitcher mouse: accumulation of galactosylsphingosine and pathology of the sciatic nerve. *Brain Res.*, **454**, 340–346.
42. Yoshimura, T., Kobayashi, T., Shinnoh, N. and Goto, I. (1990) Accumulation of galactosylsphingosine (psychosine) does not interfere with phosphorylation and methylation of myelin basic protein in the twitcher mouse. *Neurochem. Res.*, **15**, 963–967.
43. Kobayashi, T., Goto, I., Yamanaka, T., Suzuki, Y., Nakano, T. and Suzuki, K. (1988) Infantile and fetal globoid cell leukodystrophy: analysis of galactosylceramide and galactosylsphingosine. *Ann. Neurol.*, **24**, 517–522.
44. Korn-Lubetzki, I., Dor-Wollman, T., Soffer, D., Raas-Rothschild, A., Hurvitz, H. and Nevo, Y. (2003) Early peripheral nervous system manifestations of infantile Krabbe disease. *Ped. Neurol.*, **28**, 115–118.
45. Kobayashi, S., Katayama, M., Satoh, J., Suzuki, K. and Suzuki, K. (1988) The twitcher mouse. An alteration of the unmyelinated fibers in the PNS. *Am. J. Pathol.*, **131**, 308–319.
46. Santambrogio, S., Ricca, A., Maderna, C., Ieraci, A., Aureli, M., Sonnino, S., Kulik, W., Aimar, P., Bonfanti, L., Martino, S. *et al.* (2012) The galactocerebrosidase enzyme contributes to maintain a functional neurogenic niche during early post-natal CNS development. *Hum. Mol. Genet.*, **21**, 4732–4750.
47. Luzi, P., Abraham, R.M., Rafi, M.A., Curtis, M., Hooper, D.C. and Wenger, D.A. (2009) Effects of treatments on inflammatory and apoptotic markers in the CNS of mice with globoid cell leukodystrophy. *Brain Res.*, **1300**, 146–158.
48. Suzuki, K. (1990) Myelin pathology in the twitcher mouse. *Ann. NY Acad. Sci.*, **605**, 313–324.
49. Gresle, M.M., Alexandrou, E., Wu, Q., Egan, G., Jokubaitis, V., Ayers, M., Jonas, A., Doherty, W., Friedhuber, A., Shaw, G. *et al.* (2012) Leukemia inhibitory factor protects axons in experimental autoimmune encephalomyelitis via an oligodendrocyte-independent mechanism. *PLoS One*, **7**, e47379.
50. Grossberg, A.J., Scarlett, J.M. and Marks, D.L. (2010) Hypothalamic mechanisms in cachexia. *Physiol. Behav.*, **100**, 478–489.
51. Karst, S.Y., Ward-Bailey, P.F., Samples, R., Johnson, K.R., Donahue, L.R. and Davisson, M.T. (2008) In *MGI Direct Data Submission to Mouse Genome Database*. The Jackson Laboratory, Bar Harbor, Maine. http ://mousemutant.jax.org/articles/mmrmutanttwi5j.html.
52. Ye, S., Dhillon, S., Ke, X., Collins, A.R. and Day, I.N. (2001) An efficient procedure for genotyping single nucleotide polymorphisms. *Nucleic Acids Res.*, **29**, E88-88.
53. You, F.M., Huo, N., Gu, Y., Luo, M.-C., Ma, Y., Hane, D., Lazo, G.R., Dvorak, J. and Anderson, O.D. (2008) BatchPrimer3: A high throughput web application for PCR and sequencing primer design. *BMC Bioinformatics*, **9**, 253.
54. Galbiati, F., Basso, V., Cantuti, L., Givogri, M.I., Lopez-Rosas, A., Perez, N., Vasu, C., Cao, H., van Breemen, R., Mondino, A. *et al.* (2007) Autonomic denervation of lymphoid organs leads to epigenetic immune atrophy in a mouse model of Krabbe disease. *J. Neurosci.*, **27**, 13730–13738.
55. Krasnow, S.M., Nguyen, M.L. and Marks, D.L. (2011) Increased maternal fat consumption during pregnancy alters body composition in neonatal mice. *Am. J. Physiol. Endocrinol. Metab.*, **301**, E1243–E1253.
56. Lattanzi, A., Neri, M., Maderna, C., di Girolamo, I., Martino, S., Orlacchio, A., Amendola, M., Naldini, L. and Gritti, A. (2010) Widespread enzymatic correction of CNS tissues by a single intracerebral injection of therapeutic lentiviral vector in leukodystrophy mouse models. *Hum. Mol. Genet.*, **19**, 2208–2227.
57. Visigalli, I., Ungari, S., Martino, S., Park, H., Cesani, M., Gentner, B., Sergi Sergi, L., Orlacchio, A., Naldini, L. and Biffi, A. (2010) The galactocerebrosidase enzyme contributes to the maintenance of a functional hematopoietic stem cell niche. *Blood*, **116**, 1857–1866.
58. Neri, M., Ricca, A., di Girolamo, I., Alcala'-Franco, B., Cavazzin, C., Orlacchio, A., Martino, S., Naldini, L. and Gritti, A. (2011) Neural stem cell gene therapy ameliorates pathology and function in a mouse model of globoid cell leukodystrophy. *Stem Cells*, **29**, 1559–1571.
59. Suzuki, K. (1983) The twitcher mouse. A model of human globoid cell leukodystrophy (krabbe's disease). *Am. J. Path.*, **111**, 394–397.
60. Tanaka, K., Nagara, H., Kobayashi, T. and Goto, I. (1989) The twitcher mouse: accumulation of galactosylsphingosine and pathology of the central nervous system. *Brain Res.*, **482**, 347–350.
61. Gentner, B., Visigalli, I., Hiramatsu, H., Lechman, E., Ungari, S., Giustacchini, A., Schira, G., Amendola, M., Quattrini, A., Martino, S. *et al.* (2010) Identification of hematopoietic stem cell-specific miRNAs enables gene therapy of globoid cell leukodystrophy. *Sci. Transl. Med.*, **2**, 58ra84.
62. Pellegatta, S., Tunici, P., Poliani, P.L., Dolcetta, D., Cajola, L., Colombelli, C., Ciusani, E., Di Donato, S. and Finocchiaro, G. (2006) The therapeutic

potential of neural stem/progenitor cells in murine globoid cell leukodystrophy is conditioned by macrophage/microglia activation. *Neurobiol. Disease*, **21**, 314–323.
63. Wu, Y.P., McMahon, E.J., Matsuda, J., Suzuki, K. and Matsushima, G.K. (2001) Expression of immune-related molecules is downregulated in twitcher mice following bone marrow transplantation. *J. Neuropathol. Exp. Neurol.*, **60**, 1062–1074.
64. Kagitani-Shimono, K., Mohri, I., Fujitani, Y., Suzuki, K., Ozono, K., Urade, Y. and Taniike, M. (2005) Anti-inflammatory therapy by ibudilast, a phosphodiesterase inhibitor, in demyelination of twitcher, a genetic demyelination model. *J. Neuroinflammation*, **2**, 10.
65. Taniike, M. and Suzuki, K. (1994) Spacio-temporal progression of demyelination in twitcher mouse: with clinico-pathological correlation. *Acta Neuropath.*, **88**, 228–236.
66. Kobayashi, S., Chiu, F.C., Katayama, M., Sacchi, R.S. and Suzuki, K. (1986) Expression of glial fibrillary acidic protein in the CNS and PNS of murine globoid cell leukodystrophy, the twitcher. *Am. J. Path.*, **125**, 227–243.
67. Suzuki, K. and Ohno, M. (1995) Expression of immune-related molecules in a murine genetic demyelinating disease. *Prog. Brain Res.*, **105**, 289–294.
68. Taniike, M., Mohri, I., Eguchi, N., Irikura, D., Urade, Y., Okada, S. and Suzuki, K. (1999) An apoptotic depletion of oligodendrocytes in the twitcher, a murine model of globoid cell leukodystrophy. *J. Neuropathol. Exp. Neurol.*, **58**, 644–653.
69. Nagara, H., Kobayashi, T. and Suzuki, K. (1982) The twitcher mouse: normal pattern of early myelination in the spinal cord. *Brain Res.*, **244**, 289–294.
70. Takahashi, H. and Suzuki, K. (1984) Demyelination in the spinal cord of murine globoid cell leukodystrophy (the twitcher mouse). *Acta Neuropath.*, **62**, 298–308.